12-2014

# Application of Femtosecond Laser Surface Processed Electrodes in Electrolysis of Water

Christopher K. Wilson
*University of Nebraska-Lincoln*, chris.wilson.1990@gmail.com

APPLICATION OF FEMTOSECOND LASER SURFACE PROCESSED

ELECTRODES IN ELECTROLYSIS OF WATER

by

Christopher K. Wilson

A Thesis

Presented to the Faculty of

The Graduate College at the University of Nebraska

In Partial Fulfillment of Requirements

For the Degree of Master of Science

Major: Electrical Engineering

Under the Supervision of Professor Dennis R. Alexander

Lincoln, Nebraska

December, 2014

APPLICATION OF FEMTOSECOND LASER SURFACE PROCESSED

ELECTRODES IN ELECTROLYSIS OF WATER

Christopher K. Wilson, M.S.

University of Nebraska, 2014

Advisor: Dennis R. Alexander

Femtosecond laser surface processing (FLSP) is a machining technique used to develop functionalized surfaces consisting of micro and nano-scale features. Metal electrodes processed using this technique can be used in water electrolysis to facilitate more efficient hydrogen and oxygen gas production. This thesis explores the electrochemical behavior of femtosecond laser processed 316SS electrodes in water electrolysis. The multi-scale surface structure size and separation were controlled through laser fluence and incident laser pulse count. The electrodes were studied in a three electrode electrolysis cell containing a 3M KOH(aq) electrolyte, FLSP 316SS working electrode, 316SS counter electrode, and Hg/HgO reference electrode. Through linear scan voltammetry, it was found that the FLSP electrodes reduced the voltage required to stimulate 1 A of current through the electrochemical cell by 191 mV, compared to polished 316SS.

FLSP of the electrodes enhanced electrochemical efficiency through multiple mechanisms including increased electrode surface area, increased wettability, and modified bubble production behavior. Surface area analysis was conducted using confocal microscopy and current density versus voltage plots. Plasma cleaning of a polished and FLSP electrode was utilized to study the effects of wettability. Results indicated that both surface area and wettability contributed to the voltage decrease. Tafel

analysis of the voltammetry scans indicated that the surface processing did not affect the surface chemistry of the electrodes, in regards to electron transfer kinetics. The final contribution to the voltage reduction was attributed to reduction in gas bubble size produced at the FLSP electrodes. Visual inspection confirmed that a FLSP electrode reduced the bubble diameter and bubble growth time until release from the electrode surface. Further investigation into affected bubble production of a FLSP surface is necessary to identify the full effects of bubble size and release time reduction. The electrochemical enhancements resulting from the FLSP technique show that the efficiency of a common industrial electrode material can be increased through surface structuring without the addition of surface coatings or changes in geometric area.

# Acknowledgements

I would first like to thank my advisor Dr. Dennis Alexander for taking me on as a research assistant and for his guidance throughout my time working under him. His mentoring brought many education opportunities that I would not have experienced otherwise. I would also like to thank Dr. Natale Ianno and Dr. Yongfeng Lu for serving on my committee and evaluating my work.

Thank you to Dr. Troy Anderson for the close discussions about electrochemistry, Matlab, experimental setups. Your support and feedback helped shape my understanding of the electrochemical and research world. Thank you to Dr. Craig Zuhlke for the close collaborations as well as teaching me the art of laser maintenance and femtosecond laser machining. I would also like to thank Kim Bay, John Bruce III, Nick Roth, and Nick Rowse for the collaboration during my time. It was always a pleasure to work with you.

Finally, I would like to thank my father and mother, David and Ye Wilson, for the unending love and support as well as the encouragement to pursue higher education.

# Table of Contents

# List of Abbreviations

AOM – Acousto -Optical Modulator

ASB – Above Surface Growth

BSG – Below Surface Growth

CV – Cyclic Voltammetry

FLSP – Femtosecond Laser Surface Processing

FROG – Frequency Resolved Optical Gating

KOH – Potassium Hydroxide

LSV – Linear Scan Voltammetry

MEC – Microbial Electrolysis Cell

Nd:YAG – Neodymium Yttrium Aluminum Garnet

Nd:YVO$_4$ – Neodymium Yttrium Vanadate

NHE – Normal Hydrogen Electrode

PAR – Princeton Applied Research

PEM – Proton Exchange Membrane

RF – Radio Frequency

SDG – Synchronization and Delay Generator

Ti:Sapphire – Titanium Sapphire (Al$_2$O$_3$)

# List of Figures

# List of Tables

# Chapter 1.    Introduction

## 1.1.    History

From the discovery of water electrolysis in the 1789 by Adriaan Paets van

Troostwijk and Jan Rudolph Deinman, alkaline based electrolysis has developed into a

substantial production method for high purity hydrogen and oxygen gas production[1–3]

that can be used as an alternative to fossil fuels or energy storage. Many developments

have since been made to improve the efficiency of the electrochemical process and

reduce power consumption. The first major development was the pressurized electrolysis

cell. By increasing the pressure an electrolyzer operates under, greater hydrogen and

oxygen gas production rates can be achieved with very little increase in power

consumption[2, 4, 5].

The next major step in the electrolysis industry occurred in the 1970's with the

development of proton exchange membrane (PEM) water electrolysis. An ideal PEM

electrolyzer utilizes a special polymer membrane which separates the hydrogen and

oxygen production reactions by only allowing protons to transfer through the membrane

and separating the hydrogen and oxygen gasses. This prevents oxygen from limiting the

hydrogen reaction on the opposite electrode. PEM electrolyzers also benefit from higher

operating pressures, but current membrane materials allow for hydrogen and oxygen

diffusion at high pressures. A large amount of current research has been in the

development of better polymer membranes [2, 6, 7].

Recent developments in water electrolysis have incorporated renewable energy

sources. One research topic is the use of biological samples within a microbial

electrolysis cell (MEC). An MEC uses exoelectrogenic bacteria to oxidize organic material and transfer protons through the electrolyte solution. This technology coupled with traditional electrolysis technology can greatly reduce the cost of the electrochemical process [8, 9].

Another area of development is in photoelectrochemical water electrolysis. This is type of electrolysis is based on the use of semiconductor materials with large surface areas with the goal of creating a completely "green" source of hydrogen gas [2]. A significant amount of research has focused on improving the photoactivity of certain semiconductors through doping modifications.

One research path that is currently pursued is material or surface geometry modifications of the electrodes [10–15]. The goal of this approach is to improve the efficiency of the electrode/electrolyte interface by tailoring the electrode surface for better performance, e.g. less interfacial resistance, larger surface area, enhanced nucleation sites, etc. The work that is presented in this thesis investigates the effects of the surface geometry generated from Femtosecond Laser Surface Processing (FLSP) on water electrolysis. The goal is to identify the effects that the FLSP generated micro and nanoscale structures have on water electrolysis and to determine what characteristics of these structures cause the effects.

## 1.2.    Fundamentals of Electrolysis

Water electrolysis is the splitting of water into two parts hydrogen to one part oxygen gas through the application of an electric potential [16]. When a sufficient electric potential is created between two conductors, i.e. electrodes, suspended in a conductive

aqueous solution, two simultaneous reactions begin where the water is split into hydrogen and hydroxide ions.

Pure water is a poor electric conductor; therefore an ionic solution is typically used in the electrochemical process. The ideal solute used to create an basic solution should react with water to produce hydroxide and metal ions, but the metal ions should not break down prior to the initiation of the water redox reactions [16, 17]. The breakdown of metal ions prior to the breakdown of water reduces the efficiency of the electrochemical process and could potentially generate unexpected products. Extensive explanations of ionic solutions can be found in resources by Bockris and Oldham [16, 17] The most common ionic solution used in industry is potassium hydroxide as it does not cause performance losses as found with acidic electrolytes and is more conductive than other alkaline solutions, e.g. sodium hydroxide [1, 2, 18].  The use of a more conductive electrolyte reduces the potential required to initiate the reactions with very little alteration to the solution itself. The reactions that are of interest in the overall electrochemical process are reduction and oxidation reactions.

Reduction and oxidation, or redox, reactions occur in electrolysis at the solution-electrode interface. The reduction half reaction is the transfer of an electron from an electrode to a more positively charged ion present in the solution. The oxidation half reaction is the opposite where the electron is transferred from a negatively charged ion in the solution to a more positive electrode [16, 19]. This transfer of electrons via ions completes a circuit and allows for flow of current through the solution. A diagram of this process can be found in Figure 1.
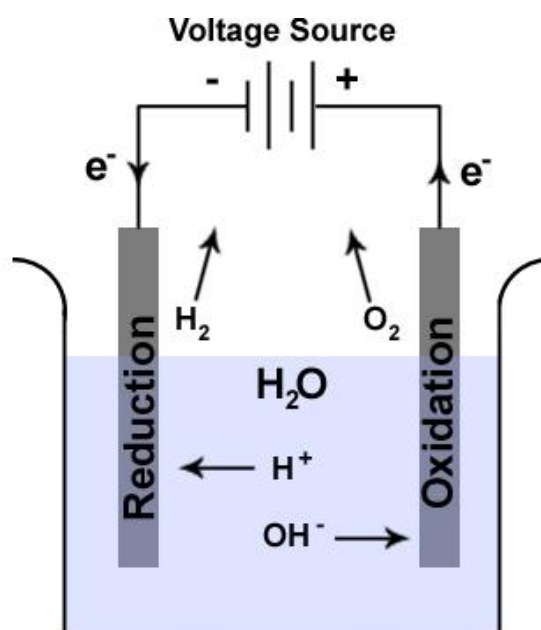
**Figure 1: Basic two electrode electrochemical cell illustrating the path of electron and ion flow necessary to complete the circuit.**

The system shown in Figure 1 is considered a two cell electrode and is a simplified representation of an industrial electrolyzer. Electrolyzers in a production environment consist of multiple plates in parallel with alternating positive and negative charges on each plate. This allows for large anode and cathodes surface areas in a compact configuration. Simplification of these systems allows for analysis of the same redox reactions that occur in production, but on a scale that does not consume the same amount of resources.

The overall chemical equation for the electrolysis of water can be described by:

$$2H_2O(l) \rightarrow 2H_2(g) + O_2(g) \tag{1}$$
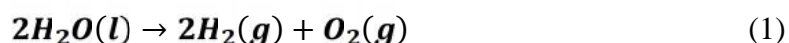
which is the overall redox reaction where hydrogen is the reduced species and oxygen is the oxidized species. Equation 1 can be broken down into the reduction and oxidation half reactions [16]. For an acidic solution, the reduction and oxidation half reactions are as follows,

$$2e^- + 2H^+(aq) \rightarrow H_2(g) \text{ (0 V vs. NHE) (Reduction in acid)} \tag{2}$$

$$2H_2O(l) \rightarrow O_2(g) + 4e^- + 4H^+(aq) \text{ (1.2288 V vs. NHE) (Oxidation in acid)} \tag{3}$$
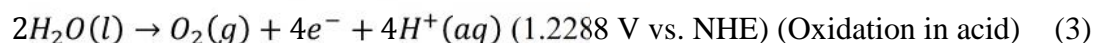
whereas the reduction and oxidation half reactions in a basic, or alkaline, solution are,

$$2H_2O(l) + 2e^- \rightarrow H_2(g) + 2OH^-(aq) \text{ (-0.8280 V vs. NHE) (Reduction in base)} \tag{4}$$

$$4OH^-(aq) \rightarrow O_2(g) + 4e^- + 2H_2O(l) \text{ (0.4008 V vs. NHE) (Oxidation in base)} \tag{5}$$
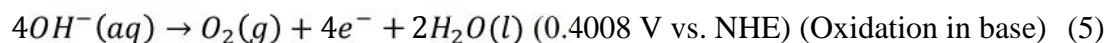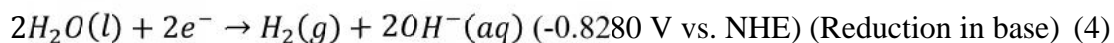
The resulting product of the two different redox reactions is the same, but the main difference is the ions used to balance the equations. An acidic solution will contain significantly more $H^+$ ions therefore the reactions will generally be controlled by Eq. 2 and 3. A basic solution is the opposite where there are significantly more $OH^-$ ions. For this discussion, Eq. 4 and 5 are most applicable as potassium hydroxide is used for the work that will be presented.

## 1.3.  Faraday's Law

As established in the previous sections, electrolysis is a chemical reaction stimulated by the application of a potential. In 1832 Michael Faraday explored this phenomenon in an attempt to quantify the amount of resulting chemical product resulting from the applied potential. It was found that the amount of electrons passing through the electrochemical cell was proportional to the amount of chemical reaction occurring, e.g. the amount of hydrogen and oxygen gas produced [16]. This relation can be represented by the following equation,

$$-N_R = N_O = \frac{Q}{nF} \tag{5}$$

, where $N_R$ and $N_O$ are the amount of reduced or oxidized species, respectively, $Q$ is the amount of charge passed, $n$ is the stoichiometric number of electrons involved in the

reaction as found in Eq. 4 and 5, and $F$ is Faraday's constant with a value of 96485

$C\ mol^{-1}$. By recording the amount of current flowing through a water electrolyzer over a

period of time, the amount of gas produced from the cell can be calculated.

Faraday's law can also be expressed as the rate at which the electrochemical reaction

occurs

$$\frac{dN_O}{dt} = -\frac{dN_R}{dt} = \frac{i}{nFA} = \frac{j}{nF} \tag{6}$$

, where $i$ is the current passing through the electrochemical cell, $A$ is the electrode surface

area interacting with the electrolyte, and $j$ is the current density. Equation 6 is important

as it introduces the electrode surface area, which is a common value for industrial

electrolyzers as increasing electrode surface area directly increases the amount and rate of

hydrogen and oxygen production [16, 20].

Eq. 6 can be used to derive a relationship between the electrochemical current and

the potential of the overall water splitting reaction and each redox reaction. The

individual redox rates $\frac{dN_O}{dt}$ and $\frac{dN_R}{dt}$ in Eq. 6 cannot be individually measured; instead the

overall net reaction rate can be measured and related back to the redox rates through the

following equation:

$$r_{net}(E) = r_{ox}(E) - r_{rd}(E) \tag{7}$$

, where $r_x$ is the potential dependent rate and the subscripts denote the net, oxidation, and

reduction reactions respectively. Equations 5 through 7 were developed based off of an

ideal system where there are no losses in the electrodes or electrolyte. Actual

electrolyzers are subject to losses, or overvoltage.

## 1.4. Overvoltage

Overvoltages in the electrochemical system increase the potential required to generate current in an electrochemical system. These overvoltages come from multiple factors that can be summarized in the following equation:

$$R_{total} = R_1 + R_{anode} + R_{bubble,O_2} + R_{electrolyte} + R_{ions} + R_{bubble,H_2} + R_{cathode} + R_2 \quad (8)$$

, where $R_{total}$ is the total resistance of the reaction, $R_1$ is the electrical resistance of the connections from the voltage source to the anode, $R_{anode}$ is the resistance of the ionic reaction at the anode, $R_{bubble,O_2}$ is the resistance from the bubbles covering the electrode surface, $R_{electrolyte}$ is the electrical resistance of the electrolyte in the electrochemical system, $R_{ions}$ is the resistance from the transfer of ions in the bulk electrolyte to the electrode, $R_{cathode}$ is the resistance of ionic reaction at the cathode, and $R_2$ is the resistance of the connects from the voltage source to the cathode [2].

The eight different resistances are typically categorized into three different overvoltages which can be classified as:

1. Ohmic overvoltage

2. Activation overvoltage

3. Concentration overvoltage

Reduction of these overvoltages leads to more efficient electrolysis.

Ohmic overvoltage is the most simple of three. It consists of $R_1$, $R_2$, and $R_{electrolyte}$, which are the electrical resistances of the solution between the electrodes and the electrical connections of the circuit. This type of overvoltage causes the most issues in experimental studies and can generate false behaviors. This can be overcome

with the use of a three electrode cell along with a Luggin-Haber capillary. This is discussed in more detail in Section 3.4.

Activation overvoltage is caused by slow kinetics of a reaction and is associated with $R_{anode}$ and $R_{cathode}$. All reactions require a certain amount of energy to begin, but any additional energy on top of that is considered activation overvoltage. This could be due to a variety of reasons, but slow transport of ions from the bulk solution and slow interactions between electrons of the ions and electrode are most significant in water electrolysis. Activation can be reduced by using a more conductive electrolyte or a more electro-active electrode to facilitate faster ion or electron transport at lower potentials.

The last type of overvoltage, concentration overvoltage, is caused by a large imbalance between ions at the surface of an electrode and in the bulk solution. This overvoltage is associated with $R_{bubble,O_2}$, $R_{ions}$, and $R_{bubble,H_2}$. As the reaction occurs, ions must transport from one electrode to the other. If there is a large imbalance between the concentration of the bulk solution and at the electrode, the transport of ions is slowed. A larger potential could be applied to drive the ions in the bulk solution to the electrode surface, but this reduces the efficiency of the process. This can be partially solved with a electrolyte with a strong concentration, but a concentration imbalance will still form if a large enough potential is applied [16, 20].

Another source of concentration imbalance between the bulk electrolyte and electrode surface is the bubbles that are generated during the process. The bubbles generated cover up a portion of the electrode until the bubble releases. This area temporarily eliminated from the reaction is absent of electrolyte and the overall ion concentration over the entire electrode is temporarily reduced. It is thought that the

functionalized surfaces that are created with FLSP can reduce the time bubbles stick to the surface, thus reducing the concentration imbalance associated with the bubbles.

## 1.5.    Motivation

The goal of the work that will be presented is to isolate and measure the impact of various FLSP modifications on electrode surfaces in alkaline electrolysis. The surface area, wettability, and conductivity of the electrode surface can be modified using the unique femtosecond laser setup and processing techniques described in Chapter 3. Modifying these parameters can reduce the overvoltage of the electrochemical system, specifically, influencing the behavior of the bubble formation.

### 1.5.1.  Alternate Techniques

Stainless steel is a common material used in alkaline electrolyzers due to low costs, but the drawback is lower electrochemical activity. This can be overcome through surface coatings that change the electroactivity of the electrode surface or create bubble nucleation sites, but the durability of this method has not been fully explored.

Many groups have applied transition metal alloys to standard electrode materials in an attempt to improve electrochemical activity [15, 21–24]. Through a study performed by C. Fan [24] of electrodeposited molybdenum and tungsten on cobalt and nickel, it was found that there was an increase electrochemical activity of the coated electrodes as compared to the bare cobalt and nickel. Through a study of long term stability, it was found that the molybdenum coated cobalt voltage was stable, varying less than 10 mV over 160 hours of applied voltage, but the molybdenum coated nickel voltage began to vary greatly after 60 hours.

M. El-Deab [25] reports the enhancement of gold, platinum, and glassy carbon electrodes with electrodeposited manganese oxide nanorods. It was found that the nanorods reduced the overpotential of the oxygen evolution reaction by 300 mV. This work is promising, but it is an expensive solution for the electrochemical industry as the enhancements found haven't been transferred to a relatively inexpensive substrate.

Research has also been conducted in areas regarding geometrically organized surface structures. Y. Huang [22] reports the enhancement of alkaline electrolysis through the use of layered porous nickel structures. It was found that the porous nickel decreased the overpotential of the electrochemical reaction as the layers of the porous structure increased, but it was also determined that the structures were not suitable for the oxygen evolution reaction. In a study performed by S. Kim [26], structured ruthenium nanorod arrays were created on nickel to explore the effects of structure height. It was found that the Ru nanorods decreased the overall reaction potential of the reaction, but the height of the densely packed nanorods did not significantly influence the reaction. This was attributed to the inability of the electrolyte to penetrate below the caps of the nanorods.

A large amount of work has also gone into simulations of electrochemical behavior changes dues to roughened or porous electrode surfaces. Compton *et al.*[27] out of Oxford, in the U.K. have studied electrode kinetics and the enhancement that is caused by a variety of surface structures. One type of structure simulated was an array of cylindrical pits in a flat surface to simulate a porous surface. As the depth of the cylinders increase, the rate and magnitude of the electron transfer that initiates the electrochemical reaction increased for both reversible and non-reversible reactions. In another study performed by

Compton *et al.*[28] simulated surface roughness by creating an array of 3D Gaussian structures extruded up from a flat surface by a specified amount. It was found that by varying the height of the 3D structures, the kinetics of the reaction could be modified. For structures with a small height value, the behavior of the electrode was found to be indistinguishable from a flat electrode, but for a structure 10 times taller, the rate of electron transfer was increased.

The work of this thesis combines the use of a common industrial electrolysis material with the surfaces that were studied by Compton. FLSP of 316SS creates structures similar to the Gaussian structures of Compton's simulations that can be used to influence surface area and wettability. It is expected that this will reduce the overvoltage of the electrochemical system. The effects of the electrode surface area, wettability, and chemical composition due to FLSP will be explored to determine the effects that each component has on the electrolysis of water.

# Chapter 2.      Electrochemical Analysis

## 2.1.   Three Electrode Cell

Electrochemical analysis of the FLSP electrodes cannot be conducted in the two electrode cell configuration as presented in Section 1.2 without large experimental error. A technique called voltammetry is typically used to isolate and study a single electrode; the working electrode. The voltage lead connected to the working electrode can be either positive or negative the reaction on the working electrode can be either the reduction or oxidation reaction, depending on the applied potential. The electrode that is not studied is called the counter electrode. The purpose of this electrode is to complete the circuit with

the power supply without limiting the kinetics of the working electrode. This type of

analysis can be applied to a two electrode cell for basic cell response to a constant

voltage, but anything more complex will have large error. A basic circuit diagram of the

two electrode cell can be found in Figure 2.
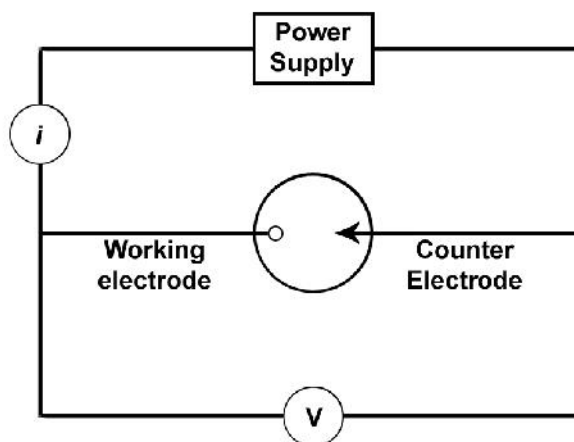


**Figure 2: Circuit diagram of a two electrode cell with working and counter electrodes along with voltmeter and ammeter used to measure cell voltage and current, respectively** [20]

In Figure 2, the voltage that is measured is the applied potential from the power

supply. The issue with this configuration for an experimental setup is related to the

voltage measurement and the effect current has as it passes through the cell. The potential

between the working and counter electrode will change as the current flow through the

cell shown in Figure 2 increases, therefore the measurement will differ from the power

supply. Many systems used to conduct voltammetry experiments will alter the voltage

applied to the cell to compensate for the difference between measured and supplied

voltage. This can cause wild fluctuations in supplied voltage as it tries to chase the

measured voltage. This can be solved using a three electrode cell.

The second type of electrochemical cell, and the one used for the experiments presented, is the three electrode cell. A circuit diagram of this type of cell can be found in Figure 3.
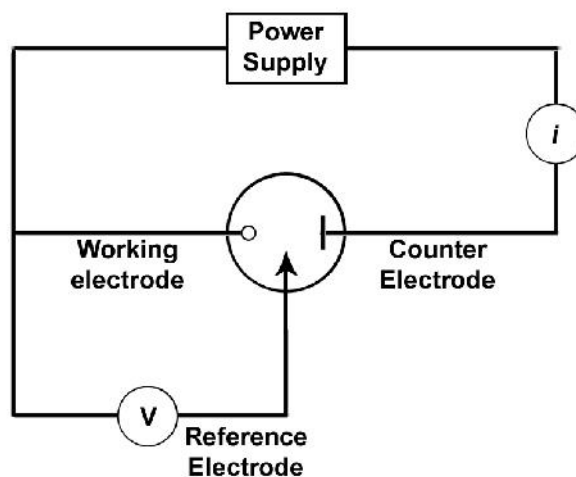


**Figure 3: Circuit diagram of three electrode cell with working, counter, and reference electrodes along with voltage and current measurement devices** [20]

A three electrode cell contains the working and counter electrodes, as found in a two electrode cell, along with a reference electrode. Like the two electrode cell, the current passes between the working and counter electrode. Unlike the two electrode cell, the measured potential of the voltmeter in Figure 3 is the potential between the working electrode and the reference electrode. An ideal reference electrode is chemically inert in that it does not participate in the chemical reactions and no current flows through the reference electrode. This three electrode setup helps improve the accuracy of the voltage measurement and control by preventing loading effects caused by current passing through the voltmeter. A typical reference electrode will have a constant and known potential value versus a set of standard, ideal electrodes [20]. These standard electrodes are known as Normal Hydrogen Electrodes (NHE).

## 2.2.    Voltammetry

Voltammetry is the study of the relationship between potential and current in an electrochemical cell [16]. This study can be used to determine various kinetic parameters of the reaction, e.g. ion transport properties, thermodynamic properties, reaction initiation, etc. The voltammetry output used for this work is called a voltammogram. An example can be found in Figure 4.
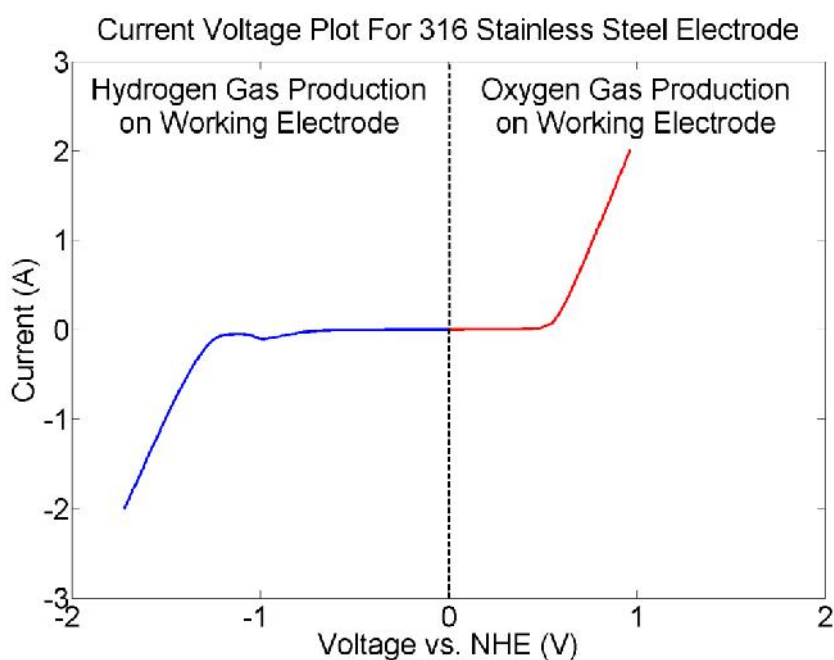


**Figure 4: Voltammogram example using an polished 316 SS plate**
The voltammogram shown in Figure 4 provides a map of the electrochemical reaction due to the working electrode/electrolyte interface. The various sections of the voltammogram can be isolated and analyzed to determine key characteristics of the electrode of interest in the hydrogen or oxygen production regime. For this work, the main voltammetry technique used is linear scan voltammetry (LSV). In LSV, the cell potential is scanned from an initial to final potential at a fixed rate as described by the following equation,

$$E(t) = E_i - vt \tag{9}$$

, where $E_i$ is the initial potential, $v$ is the user defined scan rate, and $t$ is time. This

technique can be used to determine electrochemical reactions of the electrode at high

voltages, greater than 0.5 V or less than -1 V in the sample LSV plot in Figure 4. At these

high voltages, hydrogen and oxygen gasses are produced and released from the electrode

surface, therefore performance enhancements in this region would be most applicable in

an industrial setting where the end goal is more gas production with a given set of

electrodes.

## 2.3.  Electrode Kinetics

The rate of reaction occurring on the working electrode is controlled by one or

more of the following factors [20]:

1.  Mass transfer of the transfer of ions from the bulk solution

2.  Electron transfer at the electrode, solution interface

3.  Secondary chemical reactions

4.  Surface adsorption, desorption, ect.

The two main factors that relate to the experiments presented are factors 1 and 2.

Mass transfer from the bulk solution is the simplest rate controlling process and will be

discussed first.

### 2.3.1.  Mass Transfer Limited Reactions

The rate of a mass transferred controlled reaction is entirely controlled by the rate

at which ions are brought to the surface of the electrode from the bulk solution through

migration, diffusion, or convection. At the start of the reaction on the working electrode,

the ions immediately present on the surface will be oxidized or reduced. As the reaction

continues, the surface ions will be depleted. At this point, mass transfer rate of the ions

present in the bulk solution to the electrode surface controls the overall rate of reaction. A

reaction governed by mass transfer is typically a reversible reaction. In the context of this

thesis reversibility is defined by chemical and thermodynamic reversibility as these are

most important in regards to mass transfer in water electrolysis[16, 20].

If a reaction is chemically reversible, the reactants used to create a product can be

reproduced if the chemical reaction is reversed. As an example, if water is split into

hydrogen and oxygen but no gas is produced from the electrochemical cell, applying a

sufficient reverse potential will break down the hydrogen and oxygen gas within the

electrolyte into ions which can continue to react in the cell. Thermodynamic reversibility

refers to a system in equilibrium, i.e. no reaction is occurring. A thermodynamically

reversible system means that when a small source of energy is applied to this system, a

reaction will begin to occur. If the exact opposed of the energy source is applied, the

system will react, but in the opposite direction. When a system is neither

thermodynamically or chemically reversible, it is considered irreversible.

When a reaction is chemically and thermodynamically reversible, the mass

transfer from the bulk electrolyte to a single electrode surface can be described by the

following equations

$$\frac{i}{nFA} = m_O[C_O^* - C_O(x = 0)] \tag{10}$$

$$\frac{i}{nFA} = m_O[C_R^* - C_R(x = 0)] \tag{11}$$

, where $m_O$ is the mass transfer coefficient, $C_O^*$ is the bulk concentration of the oxidized

species, $C_R^*$ is the bulk concentration of the reduced species, $C_O$ is the concentration of the

oxidized species surface of the electrode, and $C_R$ is the concentration of reduced species

at the surface of the electrode. The equation used to determine current from the mass

transfer to a single electrode is dependent on the net reaction that is occurring at that

electrode, whether that is a net reduction or oxidation reaction at the electrode.

Up until this point, a relationship has not been established between the mass

transfer rate from the bulk electrolyte to the electrode surface and the electron transfer

rate at the electrode surface. In the case of a reversible reaction as previously described,

the electron transfer rate is much greater than the mass transfer rate therefore it does not

limit the reaction. Using this idea, an equation was derived by Walther Nernst that

describes the relationship between surface concentrations of the oxidized and reduced

species on an electrode surface and the system potential. This relationship is called the

Nernst equation and is as follows,

$$E = E^0 - \frac{RT}{nF} \ln \left( \frac{C_O(x=0)}{C_R(x=0)} \right) \tag{12}$$

, where $E$ is the potential of the electrochemical cell, $E^0$ is the standard potential for the

electrode, $R$ is the gas constant with units of $Jmol^{-1}K^{-1}$, $T$ is temperature in Kelvin, and

$F$ is Faraday's constant. Using Eq. 12 along with Eq. 10 or 11, a relationship can be

found between current and potential within a reversible electrochemical reaction. If the

electron transfer rate is fast enough, the Nernst equation can be used to describe reactions

where a significate amount of current flows. A mass transfer limited reaction is typically

associated with the concentration and activation overpotential as both are affected by the

rate of ion transfer from the bulk solution. The next type of reaction limitation is mainly

associated with activation overpotential.

### 2.3.2.  Electron Transfer Limited Reactions

The second type of reaction limiting factor is electron transfer from between the

electrolyte and the electrode. The relation between applied potential and resulting current

for an electron transfer limited reaction can be determined through the use of Eq. 7. The

reduction and oxidation rates that make up the net reaction rate for a one electron reaction

on one electrode can be expressed as,

$$r_{ox}(E) = k_{ox}(E)c_R \tag{13}$$

$$r_{rd}(E) = k_{rd}(E)c_O \tag{14}$$

, where $k_{ox}(E)$ is the oxidation rate constant, $c_R$ is the concentration of the reduced

species at the electrode surface, $k_{rd}(E)$ is the reduction rate constant, and $c_O$ is the

concentration of the oxidized species at the electrode surface. The oxidation and

reduction rate constants can be expressed as

$$k_{rd}(E) = k_{rd}(E^{o\prime}) \exp\left\{-\frac{\alpha F\left(E-E^{o\prime}\right)}{RT}\right\} \tag{15}$$

$$k_{ox}(E) = k_{ox}(E^{o\prime}) \exp\left\{-\frac{(1-\alpha)F\left(E-E^{o\prime}\right)}{RT}\right\} \tag{16}$$

, where $E^{o\prime}$ is the formal electrode potential which is the measured standard potential of

each half reaction for an individual cell based off of potentials required to reduce and

oxidize a species on an electrode [29].

Through a combination of Eq. 6, 7, and 13 through 16 a relationship between current and applied potential can be developed. This equation is called the Butler-Volmer equation and is as follows

$$i = nFk^{0'} \left[ c_R \exp\left\{ \frac{(1-\alpha)F(E-E^{o'})}{RT} \right\} - c_O \exp\left\{ -\frac{\alpha F(E-E^{o'})}{RT} \right\} \right] \tag{17}$$

, where $k^{0'}$ is the standard rate constant derived from the rate constants for the oxidation and reduction reactions when they are equal and $\alpha$ is transfer coefficient [20, 29]. From the relation between applied potential and resulting current several factors, including the standard rate constant and symmetry factor, can be determined.

If the activation overvoltage of the reaction is large enough so that a large voltage must be applied the cell to stimulate a reaction, the first exponential within the bracketed term in Eq. 17 becomes negligible and the following equation can be used to determine the relation between applied potential and resulting current

$$i = i_0 \exp\left\{ (1-\alpha)\frac{nF}{RT}\eta \right\} \tag{18}$$

, where $i_0$ is the exchange current density and is equal to $FAk^{0'}c_o^{1-\alpha}c_R^{\alpha}$ and $\eta$ is the deviation from equilibrium potential and is equal to $E - E^{0'}$.

Eq. 18 can also be expressed as

$$\eta = \frac{2.3RT}{\alpha F}\log i_0 - \frac{2.3RT}{\alpha F}\log i = a + b \log |i| \tag{19}$$

Eq. 19 is commonly known as the Tafel equation. This is a useful equation to determine the exchange current density $i_0$. The exchange current density is the current density that is transferred between the working electrode and the electrolyte when the system is at equilibrium. If two electrodes are both used for hydrogen production, but one has an

exchange current density larger in magnitude than the other, the amount potential required to generate a current that produces gas will be reduced and the efficiency of the process is increased. This is the goal of a majority of electrode material research.

## 2.4.    Bubble Production

Visual hydrogen bubble production on the electrode surface does not begin until a certain voltage is reached. As the voltage between the working and reference electrode is driven to more negative values, the hydrogen ions immediately on the surface of the electrode take part in the reduction reaction forming hydrogen gas molecules. This is represented by the small peak highlighted in Figure 5.
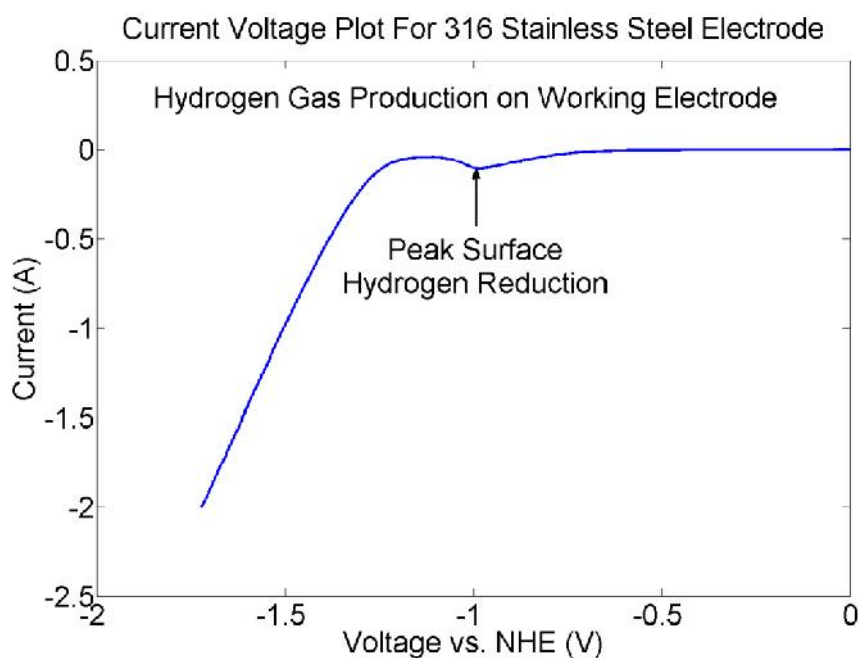


**Figure 5: Peak surface hydrogen ion reduction on polished 316 stainless steel electrode**

Visible bubble production does not begin until the linear region, starting at -1.3 V in Figure 5, is reached. At this point, the solution directly on electrode surface is supersaturated with hydrogen and visible bubbles begin to nucleate [30]. Initially, for

stagnant electrolytes, the bubbles stick to the surface of the electrode until the bubble is sufficiently large enough for buoyancy forces to overcome the force causing the bubble to stick to the surface. Once the initial bubbles release, subsequent bubbles are release through a combination buoyancy forces and micro-circulation resulting from previous bubbles floating up through the solution [31, 32].

According to Equation 18, the surface area is directly proportional to the current where a decrease in surface area would lead to a decrease in resulting current. During the bubble production in the linear section of Figure 5, the hydrogen bubbles sticking to the surface cover a certain amount of area essentially eliminating it from the electrochemical process and manipulating the current. The resulting current density during bubble production can be described by the following equation

$$j = \frac{i/A}{1-\Theta} \tag{20}$$

where $\Theta$ is the fractional bubble coverage of the electrode [31, 33].

The fractional bubble coverage is determined by the time average of the total number of bubbles covering the electrode and the average area that each bubble covers. The fractional bubble coverage can be calculated through the following equation

$$\Theta = \frac{n}{A} \int_0^{t_r} \pi (KR)^2 \frac{dt}{t_r} \tag{21}$$

where n is the number of bubbles in contact with the electrode surface, $t_r$ is the residence time of the bubble, R is the radius of the bubble of the bubble as it grows, and K accounts for the contact angle of the bubble. For electrolyte/electrode contact angles greater than 90°, the K of the bubble on the electrode is related to the contact angle of the solution on the electrode by $\sin(\phi)$ where $\phi$ is the contact angle of the electrolyte solution on the

electrode. For liquid contact angles less than 90°, the K value of the bubbles is equation

to 1. When the liquid contact angle is less than 90°, the bubbles that form shadow the

area underneath the bubble shadowed from the reaction, as shown in Figure 6.
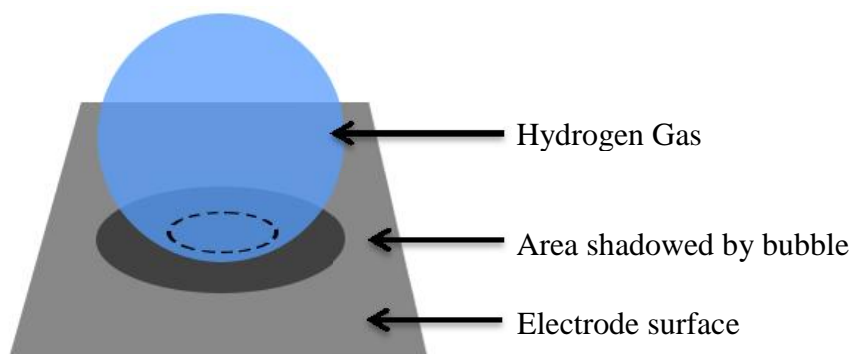


**Figure 6: Area shadowed by hydrogen gas bubble on electrode surface where electrolyte/electrode contact angle is less than 90°**

For the work in the studies presented, the contact angle of all electrodes was less

than 90°, therefore the K value of the bubbles was unity. By integrating Equation 21 over

time, the fractional bubble cover can be reduced down to

$$\Theta = \frac{\pi}{2}\frac{n}{A}R_r^2 \tag{22}$$

where $R_r$ is the bubble radius at release from the surface. The effects of the bubbles

covering the electrode can be minimized if the radius of the bubbles upon release can be

controlled. According to Vogt [31], the bubble diameter depends on the structure of the

sites the bubbles form on. Bubble diameter upon release is also dependent on the

wettability of the surface where the breakoff diameter is directly proportional to the

contact angle between the electrolyte and electrode.

# Chapter 3.    Equipment

## 3.1.    Spectra-Physics Femtosecond Laser System

The system used to develop the electrodes for this work was a combination of a

Spectra-Physics Spitfire amplifier system along with a Spectra-Physics Tsunami

oscillator. An overall diagram of the system can be found in Figure 7.
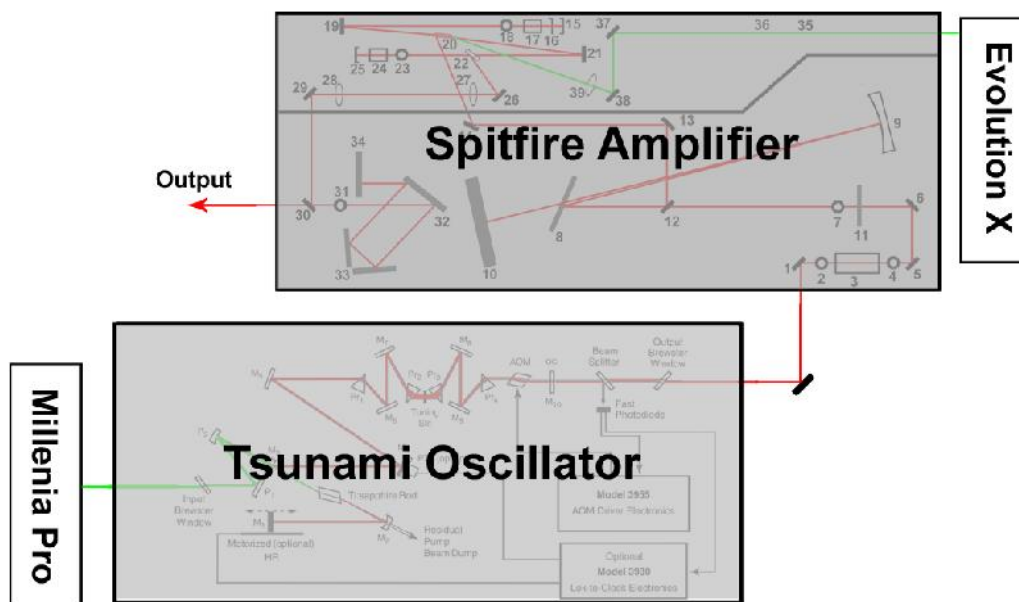


**Figure 7: Spectra-Physics femtosecond laser system with Tsunami oscillator, Spitfire amplifier cavity, and Millenia Pro and Evolution X pump lasers** [34, 35]

This system is unique in that the output is a train of ultra-short pulses on the order of

$10^{-15}$ seconds. The overall optimal output of the laser system is a 1 kHz pulse train of 50

fs pulses with peak pulse energy of 1 mJ. This pulse output is created through a series of

components all tuned to work together. The components and corresponding laser

principles will be explained.

### 3.1.1. Tsunami Oscillator

The oscillator used in this system is a Spectra-Physics Tsunami. This system is capable of producing an 80 MHz pulse train with a pulse width of about 80 fs and peak energy of 5.6 nJ. The output wavelength is centered around 800 nm and the laser is pumped with a 5 W, 532 nm Spectra Physics Millennia Pro laser. A diagram of the laser cavity can be found in Figure 8 and a list of labeled components can be found in Table 1.
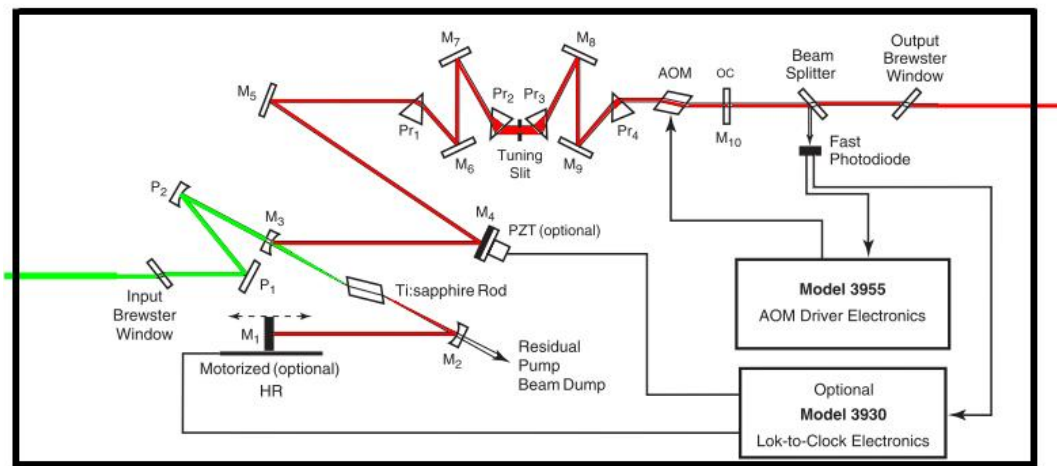


**Figure 8: Spectra-Physics Tsunami oscillator cavity diagram for femtosecond configuration** [34]

**Table 1: List of optical components in Tsunami oscillator for femtosecond configuration** [34]

| Diagram Label | Component Description |
|:---:|:---:|
| $P_1$ | Pump turning mirror |
| $P_2$ | Pump turning and focusing mirror |
| $M_1$ | End mirror |
| $M_2$, $M_3$ | Beam turning and focusing mirror |
| $M_4$, $M_5$, $M_6$, $M_7$, $M_8$, $M_9$ | Turning mirror |
| $M_{10}$ | Output Coupler |
| $Pr_1$, $Pr_2$, $Pr_3$, $Pr_4$ | Prism |

As shown in Figure 8, the 532 nm pump beam is directed in from the left side of the diagram. $P_1$ and $P_2$ direct the pump beam into $M_3$ which focuses the beam into the Ti:sapphire crystal, or the gain medium. The Ti:sapphire crystal then absorbs the 532 nm light and emits 800 nm light [34]. Figure 9 shows the absorption and emission curves for the Ti:sapphire crystal.
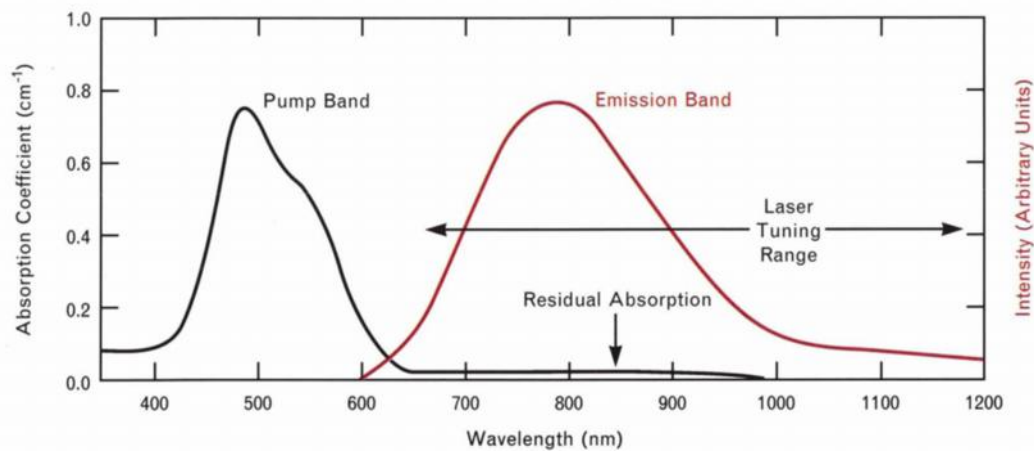


**Figure 9: Ti:sapphire crystal absorption and emission frequency curves with the range of tunable emission frequencies** [36]

From this point on, the light interacting with the optics is centered around 800 nm. The beam is then directed through the laser cavity which is composed of mirrors 1 through 10, the Ti:sapphire crystal, prisms 1 through 4, and the acousto-optical modulator (AOM). The beam continuously travels throughout the cavity and only a small portion passes through the output coupler [34].

The main purpose of the oscillator is to create a mode-locked pulse train that is supplied to the Spitfire. The input beam into the Tsunami is a continuous beam; therefore a mechanism must occur within the Tsunami to create a pulsed, mode-locked beam. There are multiple methods in which mode-locking can occur, but the goal is to phase-

lock the longitudinal modes of the beam [34, 37]. The mode-locking method used by the Tsunamic oscillator is active mode-locking.

Active mode-locking utilizes a phase or amplitude modulator to compensate for differences in frequency between modes. This compensation allows for constructive interference between certain modes creating a high powered pulse [37]. The Tsunami system modulates mode phases with the AOM. This type of modulator typically contains a quartz block with a transducer bonded to a side parallel to the laser beam path. An input radio frequency (RF) signal is passed from the transducer into the quartz creating a standing acoustic wave. This wave creates a "time-dependent" refractive index grating in the quartz [34]. This grating then diffracts a portion of input light and changes the phase of the diffracted portion.

Setting up a standing wave within the quartz and diffracting the light continuously still does not create a mode-locked beam, but by modulating the AOM transducer on and off the grating can created and destroyed and the light is not always diffracted and phase changed. The modulation creates a train of diffracted light and the phase change in said light allows for constructive interference with other modes. This results in a pulsed-mode-locked output of the oscillator [34].

The Tsunami system is wavelength tunable so the mode-locked output can be centered over a range of frequencies. This tuning is performed with the prisms and tuning slit. The beam spectrum is expanded out in space and this expanded beam is passed through the tuning slit. By adjust the width and position of the tuning slit, certain wavelengths of light can be physically blocked by the edges of the slit. This allows for full control over the frequencies present in the output beam.  The output frequency is

monitored with an Ocean Optics USB 2000 Spectrometer. An example of the resulting

mode-locked output frequency as seen by the spectrometer can be found in Figure 10.
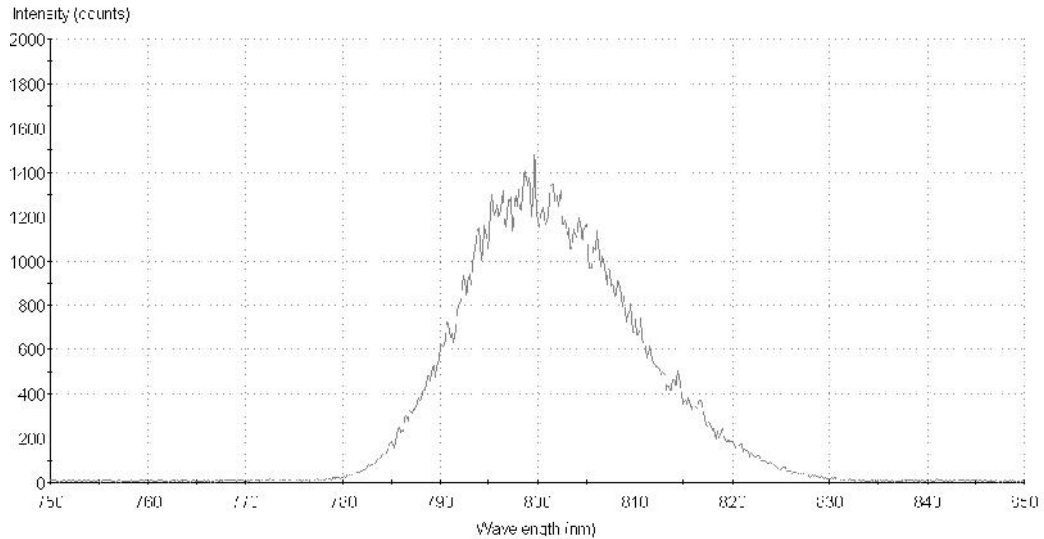


**Figure 10: Mode-locked Tsunami oscillator spectrum centered over 800 nm**

### 3.1.2. Spitfire Amplifier

The amplifier system is designed to boost the power of the oscillator signal

without damaging internal components. The amplifier can be split into three sections: the

stretcher, regen amplifier, and compressor. All of these sections work together to

manipulate the oscillator output, or seed pulse, into the Spitfire output that has 1 mJ peak

energy, 1 kHz repetition rate, and 50 fs pulse width [35]. A diagram of the Spitfire cavity

can be found in Figure 11 and a list of optical components as labeled in the diagram can

be found in Table 2.
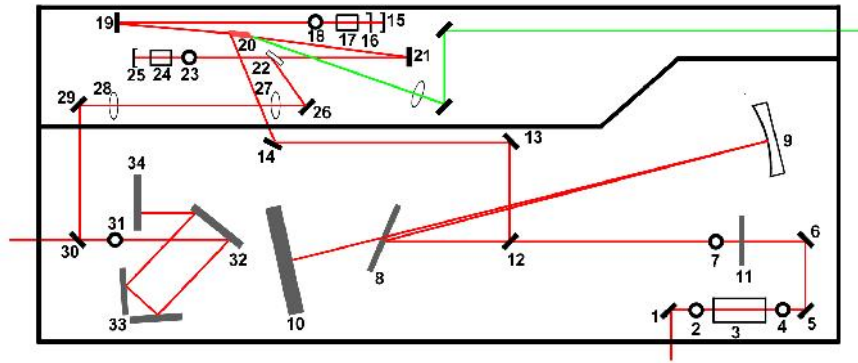
**Figure 11: Spitfire laser cavity** [35, 38]

**Table 2: List of Spitfire optical components as numbered in laser cavity diagram**
[35, 38]

| Component # | Component Name |
| --- | --- |
| 1 | Dielectric HR Mirror, 750-900 nm, 1" 45° |
| 2 | Mechanical Iris |
| 3 | Faraday Isolator |
| 4 | Mechanical Iris |
| 5 | Dielectric HR Mirror, 750-900 nm, 1" 45° |
| 6 | Dielectric HR Mirror, 750-900 nm, 1" 45° |
| 7 | Mechanical Iris |
| 8 | Spectragon Grating, 30x110x16 mm, 1200 line/mm |
| 9 | Mirror, 6", f=36" Reflective Gold |
| 10 | 1"x7" Dielectric HR Mirror, 750-900 nm, 0° |
| 11 | 1"x3" Dielectric HR Mirror, 750-900 nm, 45° |
| 12 | 1"x1" Dielectric HR Mirror, 750-900 nm, 45° |
| 13 | Dielectric HR Mirror, 750-900 nm, 1" 45° |
| 14 | Dielectric HR Mirror, 750-900 nm, 1" 45° |
| 15 | CVI Resonator End Mirror, +90 cm HR, 0° |
| 16 | 1/4 Wave plate, 0 order QWPO-825-05-4 |
| 17 | Input Sol Gel Pockel Cell, 700-1000 nm |
| 18 | Mechanical Iris |
| 19 | Dielectric HR Mirror, 750-900 nm, 1" 0° |
| 20 | 1/4"x1" Ti: Sapphire Rod |
| 21 | Dielectric HR Mirror, 750-900 nm, 1" 0° |
| 22 | Kimetic BB Output Polarizer, TFPK, 528-RW-28 |
| 23 | Mechanical Iris |
| 24 | Output Sol Gel Pockel Cell, 700-1000 nm |
| 25 | CVI Resonator End Mirror, +90 cm HR, 0° |
| 26 | Dielectric HR Mirror, 750-900 nm, 1" 0° |
| 27 | Lens, -50 mm, BB, KPC040 AR.16 |
| 28 | Lens, +400 mm, BB, KPX115 AR.16 |
| 29 | Dielectric HR Mirror, 750-900 nm, 1" 45° |
| 30 | 1"x1" Dielectric HR Mirror, 750-900 nm, 45° |
| 31 | Mechanical Iris |
| 32 | Richardson Grating, 30x110x16 mm, 1500 line/mm |
| 33 | 1.5"x3" Dielectric HR Mirror, 750-900 nm, 45° & 1.5"x2" Dielectric HR Mirror, 750-900 nm, 45° |
| 34 | 1"x3" Dielectric HR Mirror, 750-900 nm, 45° |

The first section that the seed pulse interacts with is the stretcher cavity. The purpose of this section is to stretch each pulse in time from the femtosecond scale to nanoseconds. Neglecting this step could damage the crystal in the amplifier cavity. The next section is the regen amplifier cavity where energy is added to the pulses. This is performed with the help of the Spectra-Physics Evolution X Nd:YVO$_4$ pump laser with a 8 W, 532 nm pump laser. The output from the Evolution X laser is pulsed at 1 kHz with the help of an AOM which controls cavity loss. By routing the Evolution X output into another Ti:sapphire crystal (Part 20) in the Spitfire regen amplifier cavity, the 532 nm laser light is transformed into 800 nm light.

The beam is amplified through careful alignment of the seed beam and pump beam along with the assistance of two Pockel cells (Parts 17 and 24). A Pockel cell is a crystal in which a refractive index change is induced through application of a high voltage potential. The addition of a quarter-wave plate (Part 16) allows for control over the polarization of the beam. If no voltage is applied across the Pockel cell 17, the seed beam enters the amplifier cavity, passes through Pockel cell 17 and waveplate 16, but goes no further. When a voltage is applied to the Pockel cell, the seed beam continues on through to the mirror and reflects back through the Pockel cell into the cavity. Using a Spectra-Physics Synchronization and Delay Generator (SDG), the timing of the seed pulses allowed through the Pockel cell can be controlled to align with the pulses of the Evolution X pump beam [38].

Now that the seed beam has passed through the first Pockel cell, it must pass through the cavity to be further amplified. The setup used allows for three to four passes before allowed out of the cavity. The beam is allowed out of the cavity through a second

Pockel cell (Part 24). Every time the beam passes through the cavity, it passes through an output polarizer (Part 22). The resulting polarization from the first Pockel cell allows the beam to pass through the output polarizer unaffected. An applied voltage to the second Pockel cell will change the seed beam polarization so that the pulse is reflected out of the cavity by the output polarizer. The second Pockel cell timing is also controlled through the SDG so that the beam can be amplified to a desired amount before exciting the cavity [38].

The final section that the now amplified beam passes through is the compressor. This takes the time stretched beam and compresses it from a nanosecond wide pulse to a femtosecond wide pulse, ideally 50 fs. The compression occurs with another gradient (Part 32), similar to the stretcher gradient. The time compression is finely controlled through a pair of mirrors situated on a motorized stage (Part 33). A Frequency-Resolved Optical Gating (FROG) is used to monitor the resulting beam spatial and time compression and assist with the tuning of the mirrors. The goal is to eliminate chirp, i.e. the change in frequency over time that results from a slightly detuned compressor [38].

## 3.2.    Femtosecond Laser Surface Processing

The femtosecond laser surface processing (FLSP) of the samples used for this work was carried out using the setup shown in Figure 12.
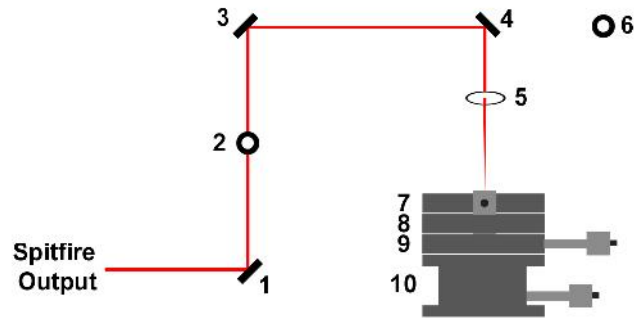
**Figure 12: Femtosecond laser machining setup configured for machining with a Gaussian beam**

The power of the beam fed into the machining setup was controlled with the

combination of a quarter-waveplate along with a polarizer. Rotation of the quarter

waveplate adjusts the polarization of the beam and the polarizer allows for the portion of

the beam polarized parallel to ground to continue onto the machining setup while remain

polarized light is blocked. A list of the components used in the setup can be found in

Table 3.

**Table 3: List of components used for the femtosecond laser machining**

| Component # | Component Name |
|---|---|
| 1 | Dielectric HR Mirror, 720-880 nm, 1" 45° |
| 2 | Mechanical Iris |
| 3 | Dielectric HR Mirror, 700-900 nm, 1" 45° |
| 4 | Dielectric HR Mirror, 700-900 nm, 1" 45° |
| 5 | Lens, +125 mm, PLCX-25.4-64.4-UV |
| 6 | WinCamD 14-bit CCD Beam Profiler, 350-1150 nm |
| 7 | Melles Griot, Nanomotion II, Horizontal, Linear Stage |
| 8 | Melles Griot, Nanomotion II, Horizontal, Linear Stage |
| 9 | Melles Griot, Nanomotion II, Horizontal, Linear Stage |
| 10 | Melles Griot, Nanomotion II, Vertical, Linear Stage |

A Gaussian beam is used to create the sufaces of interest on the samples. By focusing the beam using component 5, unique processes are introduced to the sample surface to create a micro and nano-scale structured surface. The types of surface structures formed are dependent on laser fluence, or the average laser power per beam area, and the laser pulse count, or the number of laser pulses exposed to the sample surface. Adjusting these parameters allows for the creation of a variety of surface structures including what are known as below surface growth (BSG) mounds, above surface growth (ASG) mounds, and pyramids [39, 40], which are unique to femtosecond laser processing. An example of each can be found in Figure 13.



a.                              b.                              c.
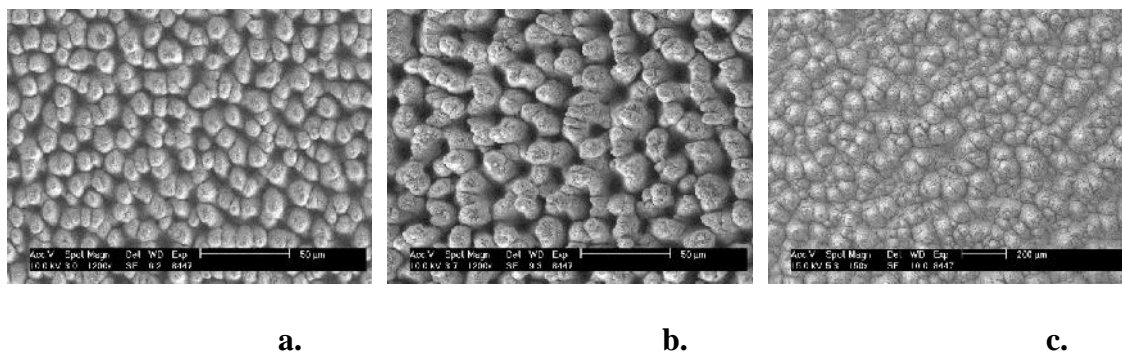
**Figure 13: Examples of a.) BSG mounds, b.) ASG mounds, and c.) Pyramids formed on the surface of 316SS using a femtosecond laser**

For this study, BSG mounds of Figure 13 a.) were created on all sample surfaces. BSG mound formation starts with the formation of random nanostructures at ~50 laser pulses incident to the sample. As the number of laser pulses increase, these nanostructures cause an increase in light scattering, which creates a new set of random nanostructures in place of the old but with an increases particle density. This cycle continues as the pulse count increases until micro scale structures begin to form out of micro ripples that develop along with the nanostructures.

From this point forward, preferential valley ablation begins to take over where the newly emerging microstructures scatter light so that there is greater laser fluence in the regions between the microstructures. This induces strong ablation effects between the microstructures. As the structures become more defined, the preferential valley ablation dissipates as the sharp angle of the valley walls have less effect on the laser fluence as compared to the previous described microstructures. At this point the structures, or mounds, grow taller and wider while the overall illuminated area is ablated further into the material. During this whole process, the structures are completely below the original flat sample surface. The height and width of the structures are then controlled through fluence and higher shot number, >200 [39, 41].

## 3.3.    Princeton Applied Research Potentiostat

As mentioned in Section 2.2, LSV can be used to determine key parameters of an electrochemical reaction on a working electrode. It would be tedious to perform these measurements manually as the potential scan ranges can be quite large, therefore a potentiostat is typically used. For the work presented, the main function of the potentiostat was to control cell voltage and monitor the resulting current. The potentiostat used for this work was a Princeton Applied Research (PAR) VersaSTAT 3A. The voltage step resolution is 30 uV $\pm$ 0.06 uV while the maximum current ranges is +/- 2A with a maximum error of $\pm$ 4 mA [42].

The benefit of using a potentiostat is that the potential ranges along with the scan ranges can be easily set, controlled, and monitored with one unit. A block diagram for the unit can be found in Figure 14.
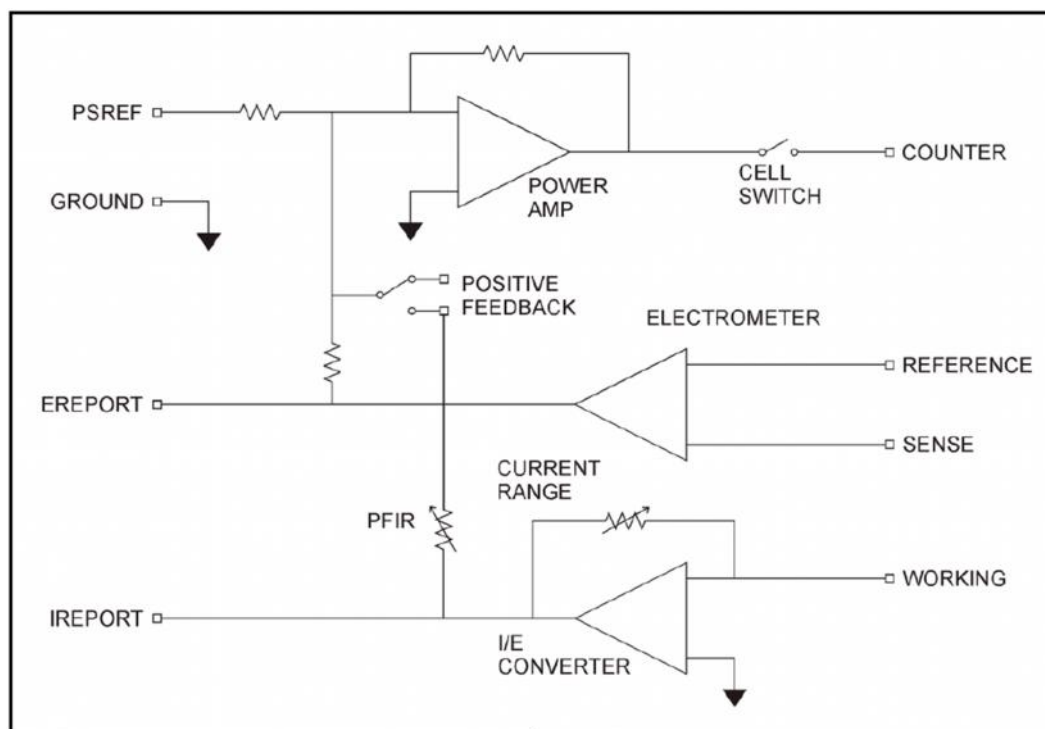
**Figure 14: Circuit diagram for PAR VersaSTAT 3A potentiostat mode** [42]

When used in the three electrode cell configuration previously described, the

working and sense leads are connected to the working electrode. The reference and

counter leads are connected to the corresponding electrode. When in operation, the

system measures the potential of the working/sense leads in respect to the reference

electrode and adjusts the potential between the counter electrode and working electrode

to bring the working electrode to the desired potential. The potential of the working

electrode with respect to the reference electrode and the current that passes through the

working electrode are then recorded [42].

## 3.4.    Electrochemical Cell

A custom electrochemical cell was used for the work presented. An isometric

rendering of the cell can be found in Figure 15.
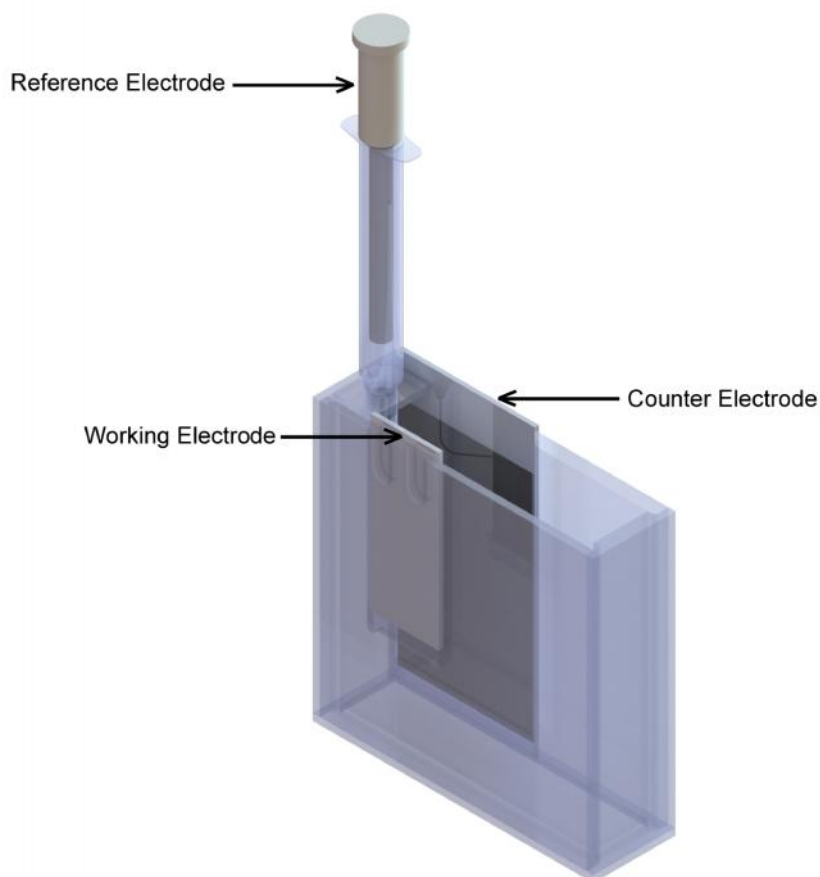
**Figure 15: Custom three electrode cell used for LSV and CV experiments with potentiostat**

The acrylic cell shown in Figure 15 was designed to constrict movement in the electrodes. Acrylic was chosen as the material for the cell as acrylic is resistant to basic solutions. The electrodes were positioned so that the center lines of the electrodes are lined up in each experiment. The cell was also designed to hold 175 mL of solution. The purpose of this specific solution volume was to keep only the FLSP portion of the working electrode in the electrolyte. The normal separation distance between the working and counter electrode surfaces was 22 mm.

The reference electrode used for this work was a CH Instruments 152 Alkaline/Mercury Oxide reference electrode with a standard voltage of 0.098 V versus a normal hydrogen electrode (NHE). The reference electrode is housed in a syringe body filled with the electrolyte and a bent needle tip is attached at the end of the body. The syringe body along with the needle tip acts as a Luggin-Haber capillary. A rendering of the reference electrode in the syringe body can be found in Figure 16.
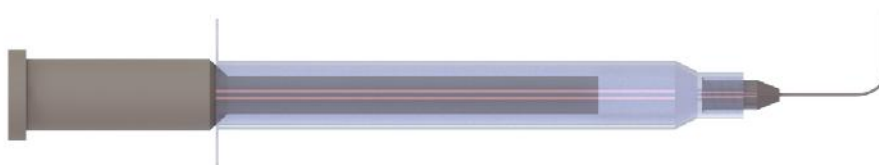


**Figure 16: CHI 152 Alkaline/Mercury oxide reference electrode in a syringe body with a bent needle tip used as a Luggin-Haber capillary**

The purpose of a Luggin-Haber capillary as set up in Figure 16 is to reduce ohmic overpotential, which is proportional to the distance between the working electrode surface and the reference electrode tip. The ideal configuration would place the tip of the reference electrode directly on the working electrode, but this is not possible with this type of configuration as the reference electrode would shield a portion of the working electrode from the reaction. The syringe body and needle help prevent shielding of the working electrode while creating a shorter path between the working electrode and reference electrode. If a Luggin-Haber capillary were not used, the uncompensated resistance would influence the potential that is measured by the potentiostat [20]. The tip was placed ~2 mm of the surface as this as any distance closer to the surface did not yield an appreciable different in results.

The electrolyte used in the custom cell was 3M KOH(aq) created used 85%

KOH(s) pellets from Sigma-Aldrich mixed with distilled water as supplied by the

University of Nebraska-Lincoln. 175 mL of the electrolyte was used to ensure that only

the FLSP portion of the electrode participated in the reaction. Once the cell was filled

with electrolyte and the electrodes placed, a 99.999% nitrogen gas flow of 60 SCCM over

the cell was started and left on for the duration of all experiments. The purpose of this

flow was to shield the electrolyte from the ambient air as KOH(aq) absorbs carbon

dioxide and water vapor. An additional flow of nitrogen gas was bubbled through the cell

to degas the solution of oxygen. The additional flow only ran when no voltage was

applied to the cell.

## 3.5.    Electrode Surface Analysis

The surface morphologies used for this work were chosen based off of

measurements taken with the help of a scanning electron microscope (SEM) and laser

confocal microscope to determine micro and nano-scale structure features such as

structure separation, height, and roughness. The following subsections will describe the

functions of each tool.

### 3.5.1.  Philips XL30 Environmental Scanning Electron Microscope

The SEM used for this work was a Philips XL30 Environmental Scanning

Electron Microscope. One benefit of using an SEM to analyze surface features is the

ability to obtain a high magnification and high resolution image that provides a 2D image

of the 3D structures that may be present on the surface. The Philips XL30 resolution has

a maximum resolution of 25 nm [41]. When using an optical microscope to study 3D

microstructure, only a portion of the sample will be in focus as each objective has a specific depth of field (DOF), or where the sample is in acceptable focus. The DOF of objectives can vary from the order of microns to millimeters.   An image of a 3D micro or nano-scale structure taken with a SEM will have the entire structure in focus at a high resolution and give a better visual representation of height through the use of contrast.

The SEM used for this work contains a tungsten filament through which a current is passed. If enough current is passed to heat up the tungsten, the filament will produce electrons. The emitted electrons can be directed through the use of electromagnetic lenses. Using a series of these lenses allows for control of electron beam collimation, diameter, focus, ect. The image output of the system is produced by backscattered electron reflection off of a conductive sample. A positively charged mesh in front of a detector directs the electrons into the detector where the electrons are measured and converted into a digital image based on the intensity of electrons. A larger image can be produced by scanning the electron beam across the sample with another set of electromagnetic lenses.

The images produced from the SEM were processed through a custom MATLAB program to determine structure spacing. The program was able to determine the structure spacing through morphological image processing and Fourier transformation. A user defined greyscale value threshold was set and used to transform the image from grayscale to a binary image. Using the image processing toolbox provided by MathWorks, the binary image was eroded to eliminate noise around the structures. A fast Fourier transform was then applied to determine the structure frequency.

### 3.5.2. Keyence VK-X200 Laser Confocal Microscope

The surface roughness and structure height were determined through the use of a laser confocal microscope (VK-X200) by Keyence. The purpose of this tool is to build a 3D composition of a surface and measure parameters from the composition. The basic operations of the VK-X200 are similar to an optical microscope. In 2D mode, only a slice of the 3D structure will be in focus as the objective focus is limited to a plane at the working distance from the objective lens. The system creates a 3D image of the structure surface through a composition of the 2D slices. The VK-X200 is capable of 0.5 nm resolution steps between each 2D slice.

One major difference between a laser confocal microscope and an optical microscope is that the laser confocal microscope utilizes a wavelength specific light source as opposed to white light. The VK-X200 uses a 408 nm light source. A confocal microscope uses this light source to illuminate the sample and monitors the back reflection off of the sample with a photoreceptor. One key feature of a confocal microscope is that a pinhole is placed in front of the photoreceptor. The optics are tuned such that light from the focal point of the beam interacting with the sample can pass through the pinhole. This means only a slice of the 3D structures imaged by the sample can be in focus at once and the remaining light is blocked out. By stepping the sample vertically and saving all of the imaged slices recorded by the photoreceptor, the composite 3D image can be created.

# Chapter 4.    Results and Discussion

## 4.1.    Surface morphologies

The overall goal of creating the structured electrode surfaces is to enhance the electrochemical process by increasing surface area, decreasing wettability, and influencing bubble behavior. The optimal functionalized surface for these enhancements was not known, therefore a series of structures were created to study the effects of structure size and spacing on the electrochemical process. In order to characterize the effect of structure size and density, two sets of electrodes were created where each parameter was varied individually. The laser fluence was varied by steps of 0.52 J/cm$^2$ to increase structure spacing and the number of shots was varied by steps of 100 shots to increase structure size. These structure characteristics were chosen in particular due to the influence on bubble formation. The studies from Vogt describe that the structure density and size would influence bubble behavior, therefore varying these parameters should change how the bubbles behave.

The surface morphologies chosen for the electrochemical experiments were chosen based off of a larger grid of surface structures created on 316 SS by varying laser fluence and incident pulse count using the laser setups described in Sections 3.1 and 3.2. The grid of surfaces created along with the selected surface is shown in Figure 17.
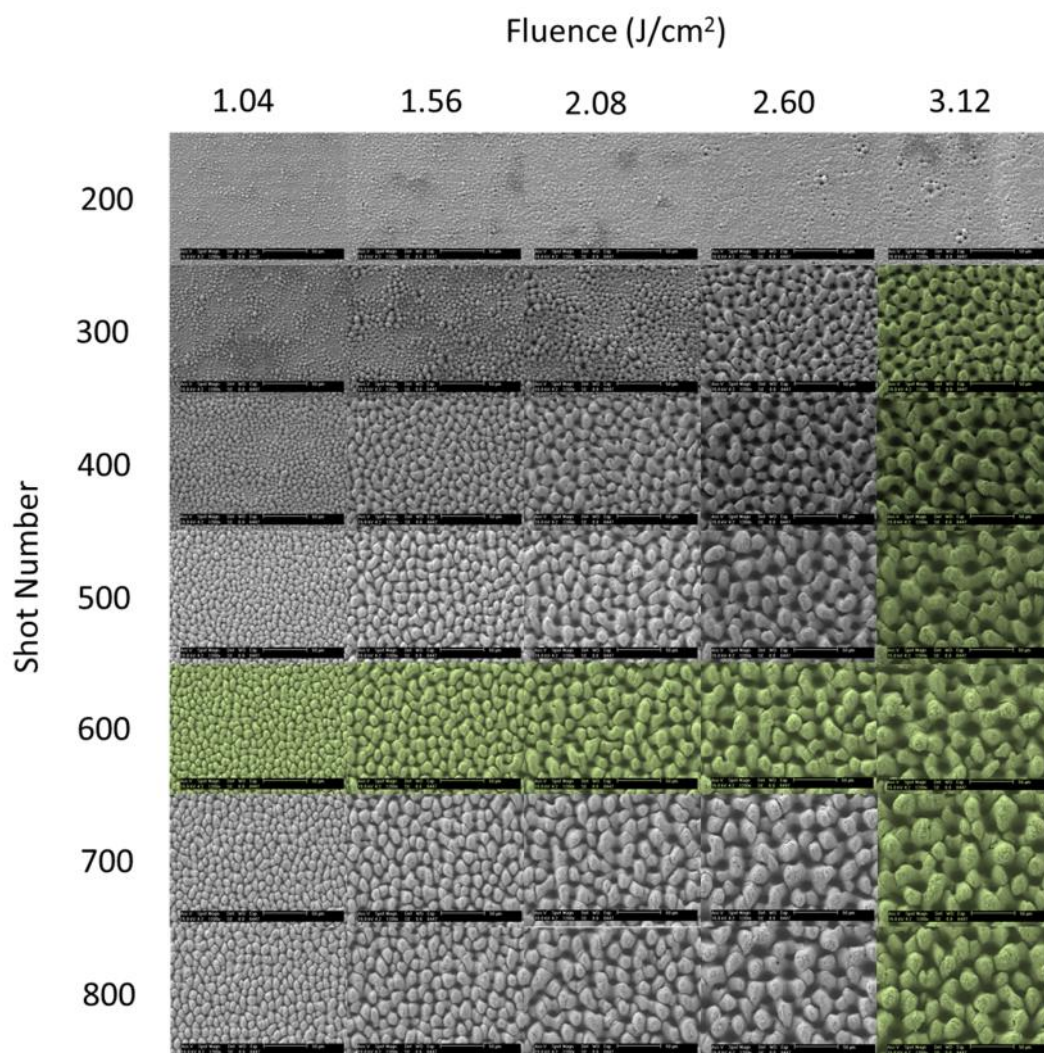
**Figure 17: Surface morphology grid created by systematically varying laser fluence and incident shot number with surface morphologies chosen for electrochemical analysis highlighted in green**

The structures where the laser shot number is held at 600 shots while the fluence

is increased from 1.04 J/cm$^2$ to 3.12 J/cm$^2$ were chosen as visually it could be seen that

the structure size and spacing grew as fluence was increased. The Matlab program used

to analyze the structures indicated the same general trend, but struggled with the

structures created at fluence settings of 2.60 J/cm$^2$ and 3.12 J/cm$^2$. This was due to the

tall "webbing" connecting the structures. The height of the webbing cause the program to

falsely identify the webbing as a structure, therefore the structure spacing measurements indicated a greater structure density, or smaller structure spacing, than what is present. The structure spacing and size measurements are presented in Table 4 and Table 5.

**Table 4: FLSP electrode surface structure peak to peak spacing (µm)**

| | | Fluence (J/cm$^2$) | | | | |
|---|---|---|---|---|---|---|
| | | 1.04 | 1.56 | 2.08 | 2.60 | 3.12 |
| Shot Number | 200 | N/A | N/A | N/A | N/A | N/A |
| | 300 | N/A | N/A | 4.352 | 7.788 | 8.221 |
| | 400 | 3.148 | 6.166 | 7.788 | 12.331 | 12.331 |
| | 500 | 4.110 | 6.726 | 8.705 | 10.570 | 14.798 |
| | 600 | 4.228 | 8.221 | 9.865 | 14.798 | 13.452 |
| | 700 | 5.103 | 9.249 | 9.249 | 13.452 | 16.442 |
| | 800 | 5.288 | 8.221 | 12.331 | 14.798 | 14.798 |

**Table 5: FLSP electrode surface average structure diameter (µm)**

| | | Fluence (J/cm$^2$) | | | | |
|---|---|---|---|---|---|---|
| | | 1.04 | 1.56 | 2.08 | 2.60 | 3.12 |
| Shot Number | 200 | N/A | N/A | N/A | N/A | N/A |
| | 300 | N/A | N/A | 3.699 | 6.726 | 5.692 |
| | 400 | 2.466 | 5.481 | 5.692 | 5.919 | 6.165 |
| | 500 | 3.794 | 3.794 | 4.624 | 4.111 | 7.046 |
| | 600 | 3.523 | 7.046 | 5.285 | 6.726 | 6.165 |
| | 700 | 3.999 | 7.788 | 4.773 | 3.999 | 5.481 |
| | 800 | 4.484 | 4.111 | 5.285 | 7.399 | 5.919 |

The red cells in Tables Table 4 and Table 5 correspond to FLSP surfaces with inconsistent or non-existent structures. These were not considered for electrochemical analysis. After the surfaces were laser processed, the samples were individually cleaned in an ultrasonic bath using distilled water for 10 minutes.

The surfaces were further studied using the Keyence VK-X200 as previously described. The purpose of this analysis was to determine surface feature height and roughness. The 3D profiles from the Keyence can be found in Figure 18.
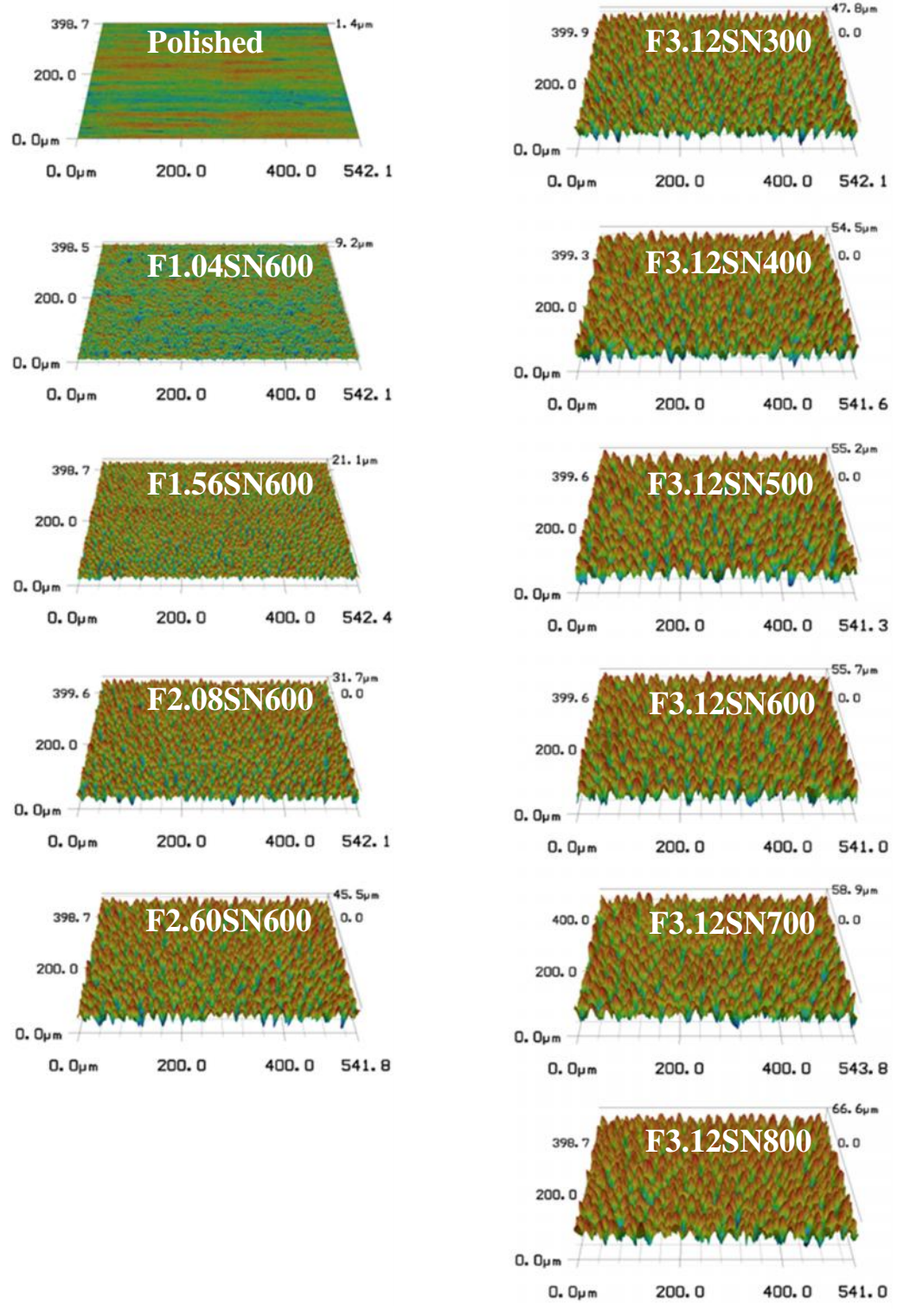
**Figure 18: 3D profiles created from laser confocal microscope scans using a 50x objective labeled with fluence and shot number settings used to process the sample**

A visual change in the surface structures for the electrodes processed with increasing fluence can be seen in the 3D profiles. A visual trend is more difficult to see in the electrodes processed with increasing shot number. The results of the measurements taken with the Matlab program and the Keyence can be found in Table 6.

**Table 6: Physical surface characteristics corresponding to FLSP electrodes derived from SEM images and 3D confocal microscope laser scans**

| Fluence (J/cm$^2$) | Shot Number | Average Peak to Valley Height (µm) | Surface Area Ratio | Structure Spacing (px) | Structure Size (px) |
|---|---|---|---|---|---|
| Polished | Polished | 0.3284 | 1.0218 | N/A | N/A |
| 1.04 | 600 | 7.0427 | 1.7672 | 4.2279 | 3.5233 |
| 1.56 | 600 | 15.8952 | 3.0456 | 8.2209 | 7.0458 |
| 2.08 | 600 | 25.0408 | 3.8960 | 9.8651 | 5.2847 |
| 2.60 | 600 | 34.4208 | 4.6298 | 14.7977 | 6.7260 |
| 3.12 | 300 | 36.7533 | 4.9373 | 8.2209 | 5.6916 |
| 3.12 | 400 | 41.7665 | 5.3673 | 12.3314 | 6.1651 |
| 3.12 | 500 | 41.0438 | 3.8320 | 14.7977 | 7.0458 |
| 3.12 | 600 | 44.4522 | 5.1547 | 13.4525 | 6.1651 |
| 3.12 | 700 | 43.3682 | 5.1781 | 16.4419 | 5.4811 |
| 3.12 | 800 | 45.7293 | 5.2442 | 14.7977 | 5.9188 |

It can be seen from Table 6 that for the electrodes processed with increasing fluence settings, the average peak to valley height, surface area ratio, average structure spacing, and average structure size increased. The average peak to valley height also increases for the electrodes processed with increasing shot number, but no general trend can be found in the surface area ratio, average structures spacing, and average structures size..

Zuhlke found that as the microstructures created on the nano-ripples were illuminated with more laser pulses, the peaks of the microstructure continued to grow and merge with neighboring structures [39]. The original sites of the microstructure still

exist, but the pits and valleys that separated the original sites are filled in or covered up by the merging structures. The incident laser shot count range explored by Zuhlke varied from 200 shots to 1000 shots increasing by steps of 100 shots.

From results presented by Zuhlke, a large visual difference existed between the small structures formed at 200 shots versus structures almost four times larger in diameter formed at 1000 shots. It is more difficult to make the same relative comparison between structures created with shot counts separated by 100 shots. It could also be seen from the Zuhlke's results that the structures created in the 400 shot to 800 shot range were very similar in structure density and size. The BSG merging mechanism along with the observations from Zuhlke's study where the structures created with steps of 100 shots do not vary greatly from the previous structure could explain why the structures created with increasing shot number used in this study do not vary greatly from each other.

## 4.2.    Electrochemical Analysis

The scans performed for the electrochemical analyses were designed to generate hydrogen on the surface of the working electrode. The resulting LSV scans from the all of the electrodes tested were created using a start voltage of 0 V. The scan was initialized with a CV scan from 0V to 0.5V then back to 0V at a scan rate of 0.01V/s. The purpose of this scan was to eliminate charge that had built up on the surface of the electrode. The LSV scan was then performed from 0V to -3V or until the 2A current limit of the VersaSTAT was met. This scan was performed at 0.01 V/s. The results of the LSV scan can be seen in Figure 19.

**Figure 19: Current vs. Potential scans for all FLSP 316SS electrodes where a.) contains the scans performed with the polished electrode and electrodes created with increasing fluence and a fixed shot number, b.) contains the detailed Zoom 1, c.) contains the scans performed with the polished electrode and electrodes created with increasing shot number and a fixed fluence, and d.) contains the detailed Zoom 2.**

From Figure 19, it can be seen that for voltages greater than 1V, there is shift of all FLSP electrodes to a less negative value as compared to the polished electrode. A general trend between increasing fluence and overall shift to the right can be seen in Figure 19 b.) where an increase in fluence used to process the electrode leads to a larger difference between the FLSP and polished electrodes. A plot shifted to towards the right of the graphs indicates that the electrode is more efficient than an electrode associated

with a plot closer to the left of the graph; a smaller potential is required to produce the same amount of current for a more efficient electrode. In the case presented in Figure 19 b.), the electrode associated with F3.12SN600 is the most efficient of all electrodes at allowing current to flow through the cell.

A trend is more difficult to see when comparing the polished electrode with those processed with increasing shot number in Figure 19 c.). From Figure 19 d.), it can be seen that the FLSP electrodes do push the linear section further to the right, but there is very little difference between the FLSP electrodes themselves. A majority of the lines fall within the error bars of the others.

The increase in efficiency of the FLSP electrodes as compared to the polished electrode could be due to the increase in surface area, decrease in wettability, change in surface chemistry of the electrodes, change in bubble production size and release behavior, or a combination of these factors. In the following sections, each factor will be isolated and analyzed individually to determine the contribution that each factor has on the efficiency increase.

### 4.2.1. Surface Area

A portion of the performance increase of the FLSP electrodes versus the polished may be partially explained by the increase in surface area. According to Faraday's law in Section 1.3, the output current is directly related to the electrode surface area. This is a common explanation to efficiency increases seen on roughed electrodes. Normalizing the current by electrode surface area using the Keyence analysis could expose other factors that are influencing the electrochemical process. Using the surface area parameter as

measured by the Keyence system, the normalized current was plotted versus the voltage.
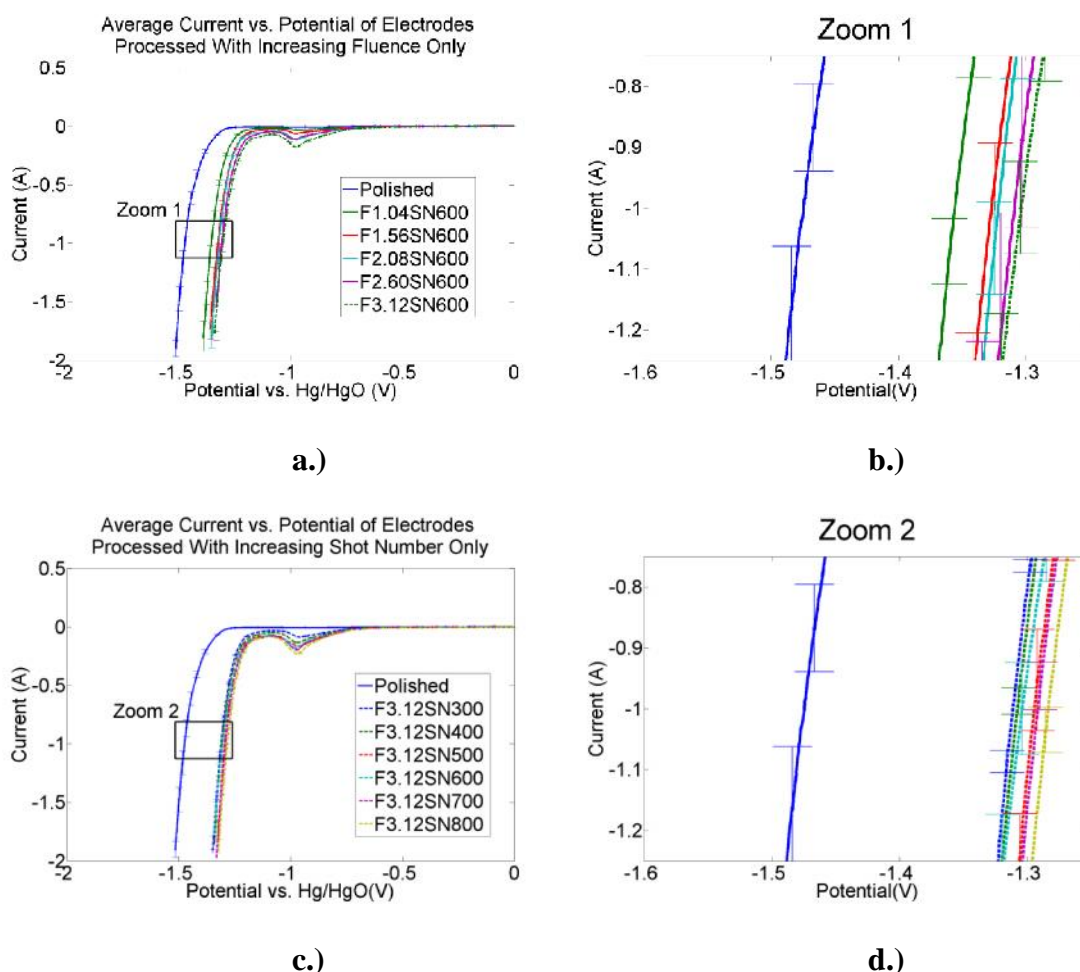
The results can be found in Figure 20.
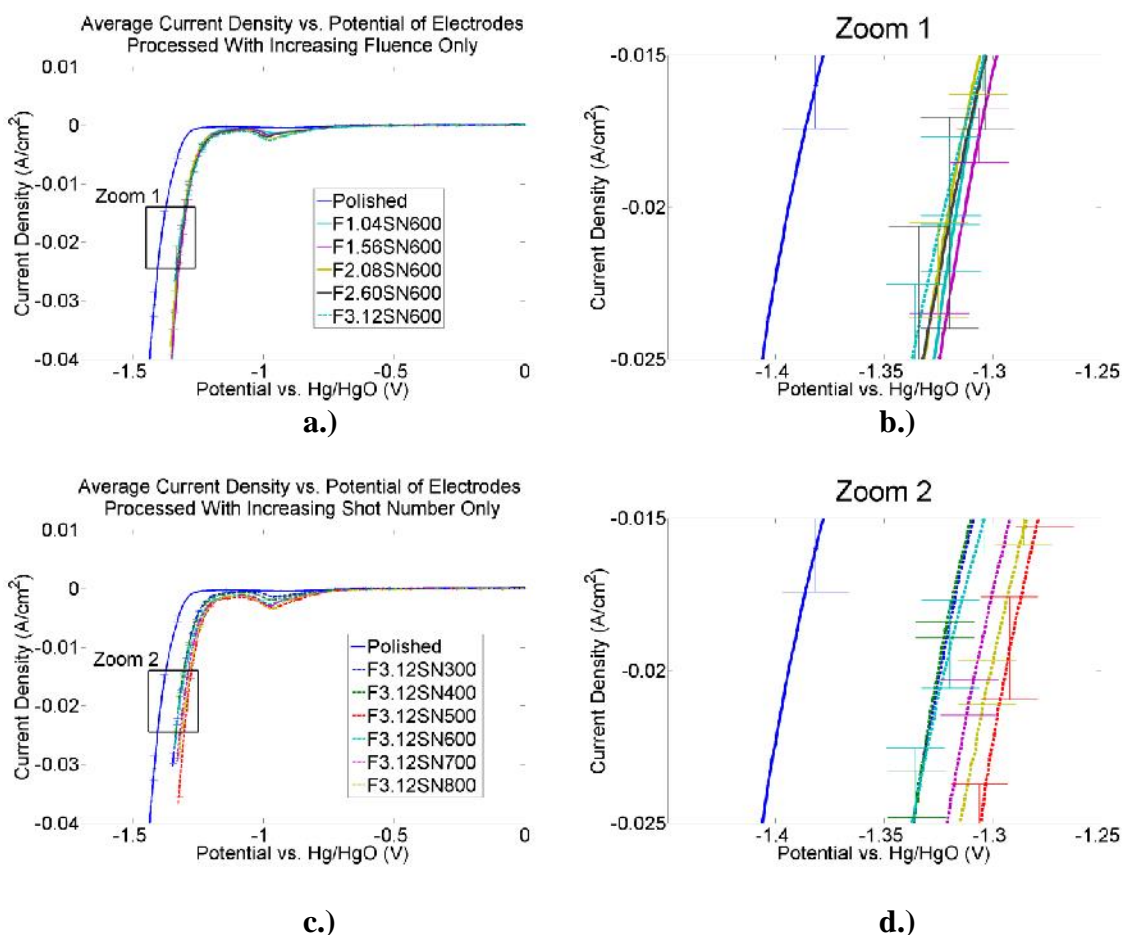


**Figure 20: Current density vs. potential scans for all FLSP 316SS electrodes where a.) contains the scans performed with the polished electrode and electrodes created with increasing fluence and a fixed shot number, b.) contains the detailed Zoom 1, c.) contains the scans performed with the polished electrode and electrodes created with increasing shot number and a fixed fluence, and d.) contains the detailed Zoom 2.**

It can be seen that when normalized by area, the FLSP electrode plots are still less

negative than the polished. Figure 20 b.) shows that the electrodes processed with a fixed

shot number and increasing fluence are virtually the same as each fall within the error

bars of the others, but overall they are better than the polished sample. Figure 20 c.)

shows that there is some difference in the performance between the electrode processed

with 3.12 J/cm$^2$, 600 shots and the electrode processed with 3.12 J/cm$^2$, 500 shots, but there is no visible trend between shot number and shift over to the right.

Error is introduced into the plots in Figure 20 as the limitations of the Keyence microscope were reached when analyzing the electrodes processed with fixed fluence and increasing shot number. Because the Keyence system operates on optical principles, highly absorbing surfaces do not return strong signals back to the photodetector. As the pits in the microstructures increased, more noise from the pits was returned back to the system. After utilizing the data processing built into the Keyence system, the noise was typically reduced down to a set level, therefore the average peak to valley height of the surfaces began to converge around 45 µm even though the only signal back from the pits was noise.

The analyses of the polished, F1.04SN600 through F2.60SN600, and F3.12SN300 through F3.12SN500 electrodes were considered correct as there was laser signal returned from the bottom of the valleys. Large error was introduced into the surface area measurements of the F3.12SN600 through F3.12SN800 due to little or no laser signal returned from the valleys. The program does not adjust for this; instead it assumed that the lowest point of the valleys is between 40 µm to 45 µm. This influences the position of the plots after normalizing the data, but it can be seen that the electrodes with strong return signals from the valleys were still shifted towards the right, and thus were more efficient than the polished electrode even after normalizing the data.

Another issue with Keyence system is inability to measure nanoscale particles as the resolution of the system is not high enough. Nanostructures are important in electrochemistry as they can be used to greatly enhance the surface area of an electrode.

Also, these nanostructures could facilitate or inhibit electron transfer, depending on the conductivity with the base material. [13, 14, 43].

Many methods are used to determine the area that participates in the electrochemical reaction, or the electrochemical surface area, but it is still a highly research topic. There is a wide variety of techniques used for different monatomic materials, but very little for alloys, especially stainless steel. [44, 45].  It was concluded that little to no nanoparticles were left on the surface after the ultrasonic bath, but nanoscale structures could still play a role in the electrolysis.

### 4.2.2.  Wettability

To determine the cause of the shift with the normalized data, a new series of tests were performed to observe the influence of surface wettability on the LSV. The FLSP electrodes were super hydrophilic with contact angles less than 5° whereas the polished electrode has a contact angle of about 35°. According to Vogt, this difference in surface wettability will play a  role in the shift of the LSV scans to less negative values [31, 33]. To test the effect of wettability without a structured surface, a polished sample was plasma cleaned in an air environment and an oxygen only environment to. The goal of the plasma cleaning was to remove any organic or carbon contaminants on the surface of the electrodes. The air plasma processing was conducted for 10 minutes and produced a surface with an average contact angle of 12.1°. The oxygen plasma cleaning was conducted for 30 minutes and produced a surface with an average contact angle of 9.8°. The results of the electrolysis performed with the plasma-cleaned electrodes can be found in Figure 21.
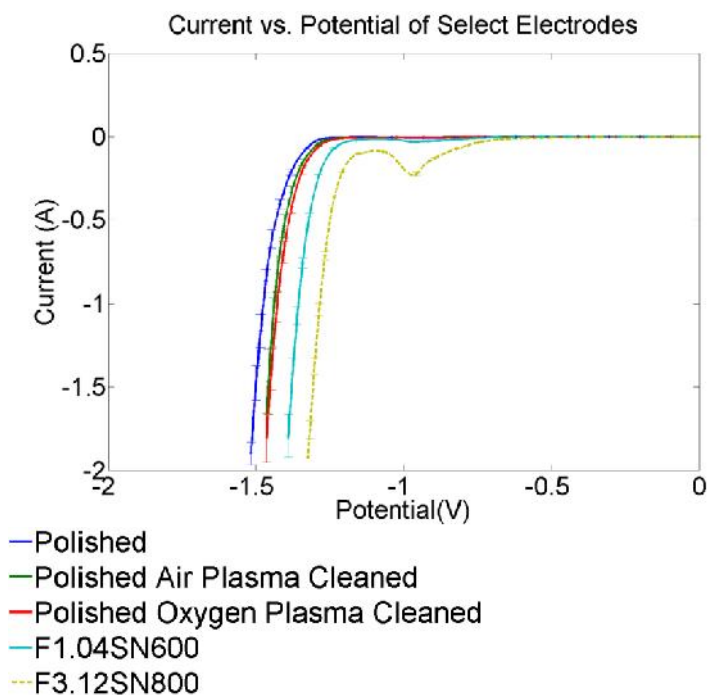
**Figure 21: Current Density/Potential scans for 316SS electrodes including the polished, air plasma cleaned, and oxygen plasma cleaned electrodes along with two FLSP electrodes.**

From Figure 21, it can be seen that the plasma-cleaned surfaces were more

efficient at producing hydrogen than the polished electrode surfaces. This enhancement

can be explained by studies conducted by Vogt [31] and Wüthrich [46] where it was

found that surface wettability decreases the contact angle of the bubbles on the surface of

the electrodes and this decrease in contact angle leads to higher resulting current densities

due to less area blocked by the hydrogen bubble.

When comparing the plasma cleaned LSV plots with the FLSP LSV plots, it can

be seen that the plasma-cleaned electrodes did not perform as well as the FLSP samples.

This may be due to a variety of factors including increased electrochemical surface area

due to nano-particles, effects of surface structure, or different surface chemistry of the

FLSP areas. Surface area of the FLSP electrodes can once again be factored out. The results of this step can be found in Figure 22.



**a.)**                                                                                              **b.)**

**Figure 22: Current density vs. potential scans for 316SS electrodes where a.) contains the scans performed with the polished electrode, plasma cleaned electrode, and worst performing FLSP electrode and b.) contains the detailed Zoom 1**

The comparison between the plasma-cleaned, polished electrode, and FLSP electrode in Figure 22 shows that removing surface carbons and lowering the contact angle of the polished electrode to 9.8° shifts the performance closer to the FLSP electrode, but the performance of the plasma cleaned, polished electrode does not match that of the FLSP electrode. Another experiment was conducted comparing a FLSP sample with a plasma cleaned, FLSP sample. The aim of this experiment was to determine if the shift seen in the plasma cleaned, polished sample was due to contact angle alone or if the reduction of surface carbons altered the electrochemical process.

The FLSP sample used for this experiment was first tested in the electrochemical cell to verify that the performance matched previous data. The contact angle was then measured and an average contact angle of 2.62° was recorded. The surface was then plasma cleaned in a pure oxygen environment for 30 minutes. Immediately after the

sample was plasma cleaned, the contact angle was once again measured with an average

contact angle of 2.67°. The next intended step was to perform the same LSV scan, but the

supporting electrolyte in the reference electrolyte needed to be replenished. A 1M

KOH(aq) solution was added to the reference electrode body, but the conductivity of this

electrolyte was higher than the existing electrolyte. This may be due to the gradual loss of

ions through the ceramic tip or Teflon body over a large number of experiments. To

overcome this issue, the plasma cleaned F3.12SN800 experiment was run followed by a

LSV experiment using the non-plasma cleaned, F3.12SN700. The performance of the

F3.12SN700 compared to the polished sample was known, therefore the performance of

the F3.12SN700 could serve as a benchmark for the plasma cleaned F3.12SN800

electrode. The results of these experiments can be found in Figure 23.



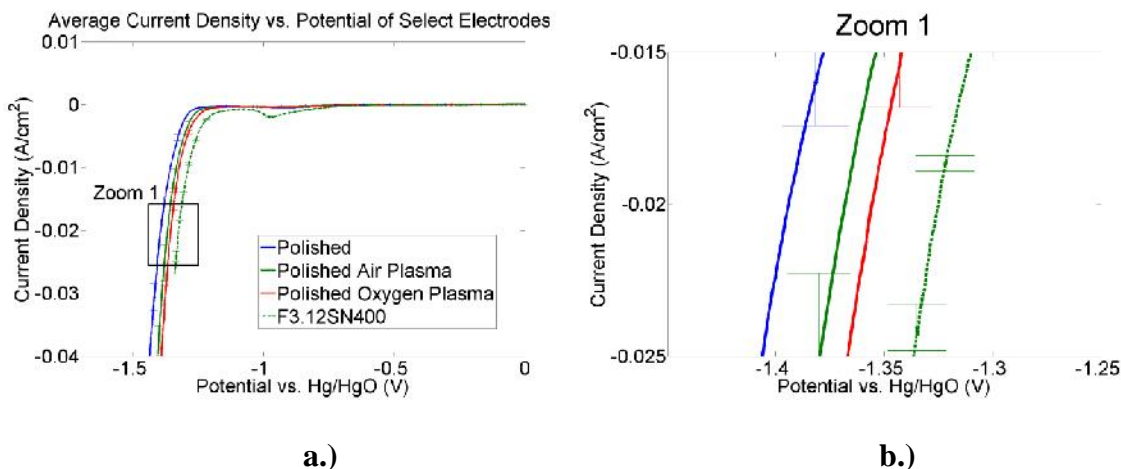a.)                                                    b.)
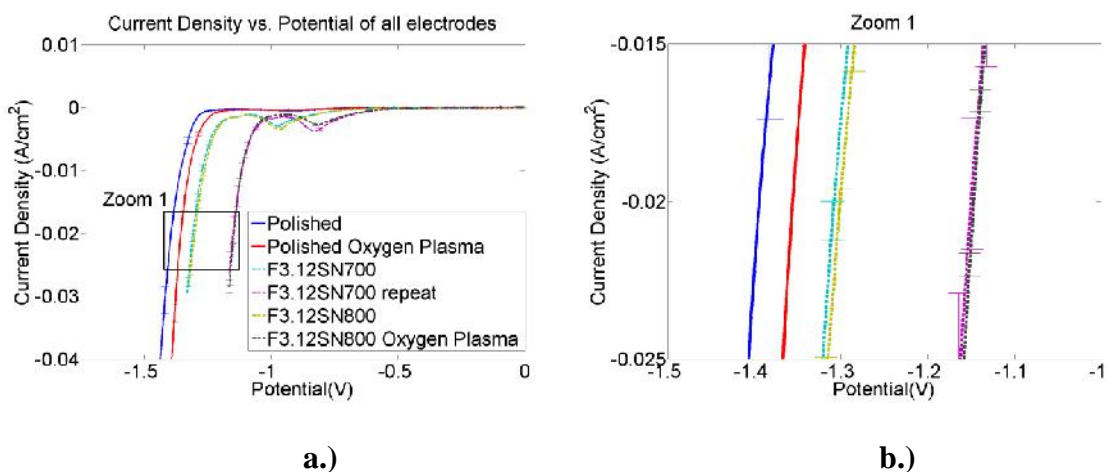
**Figure 23: Current density vs. potential scans for 316SS electrodes where a.)
contains the scans performed with the polished electrode, plasma cleaned electrodes,
and FLSP electrodes with previous reference electrode configuration, and plasma
cleaned electrodes with the new reference electrode configuration  and b.) contains
the detailed Zoom 1**

The difference in contact angle between the non-plasma cleaned, FLSP electrode

and plasma cleaned, FLSP electrode was nearly zero when accounting for the standard

deviation, therefore any difference in the LSV plots with current density would be due to the removal of the surface carbons. Figure 23 shows that there is no difference between the plasma cleaned P3.12SN800 electrode and the P3.12SN700 electrode, which fell within the deviation of the non-plasma cleaned P3.12SN800 electrode when using the previous reference electrode configuration. Figure 23 indicates that the presence of surface carbons does not produce a chemical effect on the electrochemical process beyond influencing the liquid contact angle. To ensure that this conclusion was correct and to determine if FSLP altered the surface chemistry of the 316SS beyond the original state, the surface chemical composition was investigated.

### 4.2.3. Electrode Kinetics

Analysis of the surface chemical composition could not be conducted with the electrochemical data until the rate limiting mechanism was identified. As stated in Section 2.3, the two types of rate limiting mechanisms are electron transfer limited and mass transfer limited reactions. The type of mechanism was determined through analysis of the log of current density of all electrodes plotted versus voltage, or the Tafel plot. Section 2.3.2 describes the behavior of an electron-limited reaction where the current, voltage behavior becomes linear during bubble production. Using this concept, if the Tafel plot becomes linear at large potentials where bubbles are created on the electrode surface, the reaction is electron transfer limited. Mass transfer may partially limit the reaction, but it is not significant compared to the limit imposed by the electron transfer. It was found that the Tafel plots at higher voltages became linear for the electrodes used in this study; therefore the reactions on all of the 316 SS electrodes were electron limited.

From studies conducted by Sheng [47] and Fan [24], the Tafel constant b from Equation 19 was dependent on material chemistry, therefore finding the b value from the Tafel plots of the polished and FLSP electrodes would characterize the surface chemistry of the polished and FLSP electrodes. This will help determine if the performance shifts seen in Figure 19 and Figure 22 in the FLSP electrodes are, in part, due to surface chemistry. The resulting Tafel plots for the polished and FLSP electrodes can be found in Figure 24.



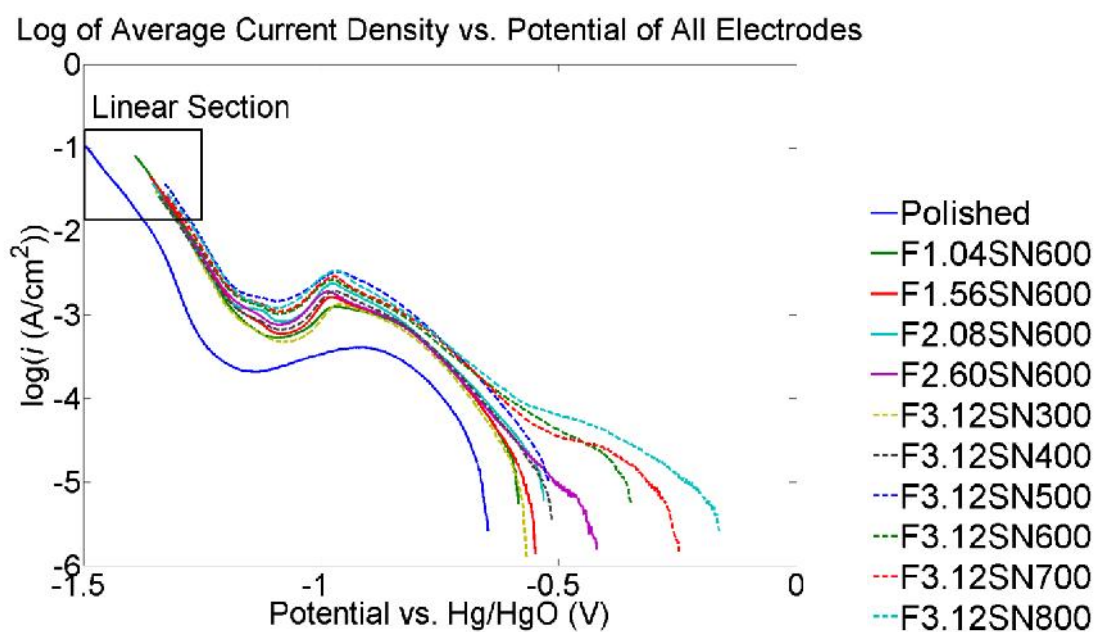**Figure 24: Tafel plots for polished and FLSP electrodes with highlighted linear section used to determine Tafel coefficients, exchange current density, and transfer coefficients**

Using the linear section highlighted in Figure 24, the Tafel coefficients a and b can be determined from the linear trend line derived from the data points. The resulting coefficient along with the log of the current density can be found in Table 7.

**Table 7: Tafel data for polished and FLSP electrodes including Tafel coefficients a and b and the log of the exchange current density**

| Fluence (J/cm$^2$) | Shot Number | b (mV/decade) | | | a (mV) | | | log(j$_0$ (A/cm$^2$)) | | |
|---|---|---|---|---|---|---|---|---|---|---|
| Polished | | -139.19 | ± | 3.38 | -1631.04 | ± | 5.01 | -11.72 | ± | 0.28 |
| Air plasma | | -120.63 | ± | 1.27 | -1573.14 | ± | 7.82 | -13.04 | ± | 0.09 |
| Oxygen plasma | | -143.92 | ± | 0.07 | -1588.08 | ± | 5.50 | -11.03 | ± | 0.04 |
| 1.04 | 600 | -143.82 | ± | 8.42 | -1549.14 | ± | 13.18 | -10.80 | ± | 0.55 |
| 1.56 | 600 | -150.74 | ± | 13.03 | -1563.27 | ± | 22.40 | -10.44 | ± | 0.86 |
| 2.08 | 600 | -141.70 | ± | 18.49 | -1557.14 | ± | 30.23 | -11.13 | ± | 1.08 |
| 2.60 | 600 | -131.96 | ± | 8.51 | -1543.72 | ± | 19.88 | -11.74 | ± | 0.62 |
| 3.12 | 300 | -135.36 | ± | 7.35 | -1553.93 | ± | 13.05 | -11.51 | ± | 0.52 |
| 3.12 | 400 | -124.44 | ± | 16.16 | -1536.45 | ± | 28.25 | -12.53 | ± | 1.45 |
| 3.12 | 500 | -136.94 | ± | 14.78 | -1523.43 | ± | 24.38 | -11.23 | ± | 0.98 |
| 3.12 | 600 | -158.26 | ± | 11.23 | -1591.26 | ± | 22.48 | -10.09 | ± | 0.55 |
| 3.12 | 700 | -141.32 | ± | 1.09 | -1547.67 | ± | 0.91 | -10.95 | ± | 0.08 |
| 3.12 | 700 (Repeat) | -128.83 | ± | 2.57 | -1368.64 | ± | 6.55 | -10.63 | ± | 0.19 |
| 3.12 | 800 | -153.31 | ± | 2.14 | -1560.68 | ± | 5.04 | -10.18 | ± | 0.11 |
| 3.12 | 800 (Plasma) | -124.56 | ± | 14.40 | -1357.73 | ± | 24.34 | -11.03 | ± | 1.09 |

From the data presented in Table 7, it can be seen that many of the average Tafel slopes and log of the exchange current densities fall within the standard deviation of the other electrodes. This indicates that the electron transfer behavior of each FLSP electrode is the same as a polished 316 SS electrode. Even both of the plasma cleaned samples exhibit similar Tafel behavior as the polished electrode indicating that the surface chemistry that is removed by the plasma cleaning does not affect the electron transfer process between the electrode and electrolyte.

The effects of the microstructure on the resulting current were explored by plotting average peak to valley height and average structure spacing versus the potential at -1 A to determine the shift in voltage for each line. The results can be found in Figure 25 and Figure 26. The results from the different reference electrode configuration were

not used as they were nearly identical with an offset as compared to the data from the

first electrode configuration.



**Figure 25: Relation between the voltage required to reach -1 A and the average peak to valley height of all electrodes including the polished, plasma cleaned, and FLSP electrodes**

**Figure 26: Relation between the voltage required to reach -1 A and the average structure spacing of all electrodes including the polished, plasma cleaned, and FLSP electrodes**

The general trend that can be seen in Figure 25 is that as the microscale structure height of the FLSP electrodes increases, the efficiency of the electrolysis also increases. A trend towards a plateau at the higher average peak to valley values may exist, but it is difficult to develop a trend line without data points beyond 50 µm. As previously mentioned, the Keyence system struggled with the peak to valley measurements when a value of around 40 µm. If the true peak to valley heights of the structures processed with increasing shot number were greater than those measured, a more obvious plateau in the data may be produced. The data presented in Figure 26 indicates that as the structure spacing of the microstructure on the FLSP sample increases, the efficiency of the process also increases. There isn't a plateau as found in Figure 25, but electrodes with larger structure spacing beyond those tested may reveal the overall trend.

The increase in efficiency seen in Figure 25 and Figure 26 could be due simply to an increase in the surface area, which would directly relate to an increase in current according to Faraday's law, or due to enhanced bubble behavior. To determine the effects of surface area in Figure 25 and Figure 26, the same plots were created with current density. The results can be found in Figure 27 and Figure 28.
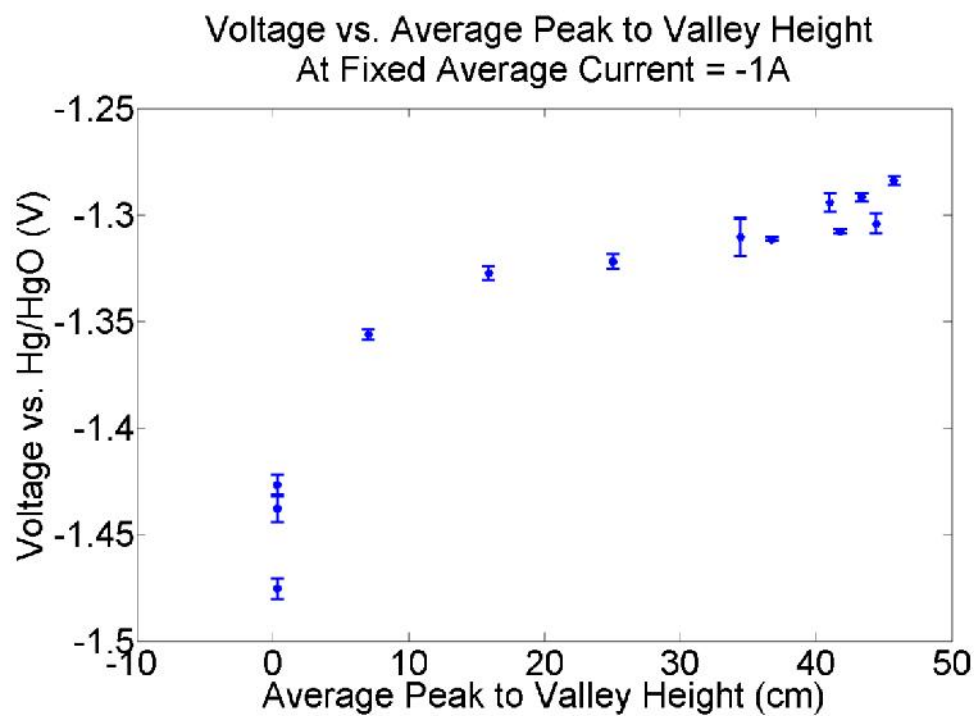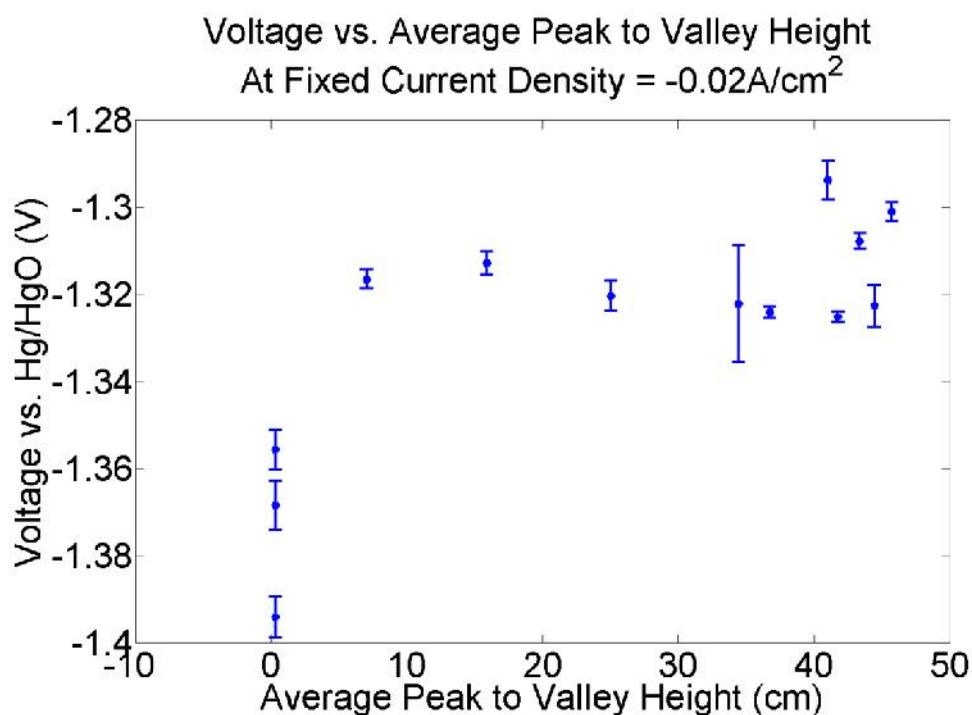


**Figure 27: Relation between the voltage required to reach -1 A/cm$^2$ and the average peak to valley height of all electrodes including the polished, plasma cleaned, and FLSP electrodes**
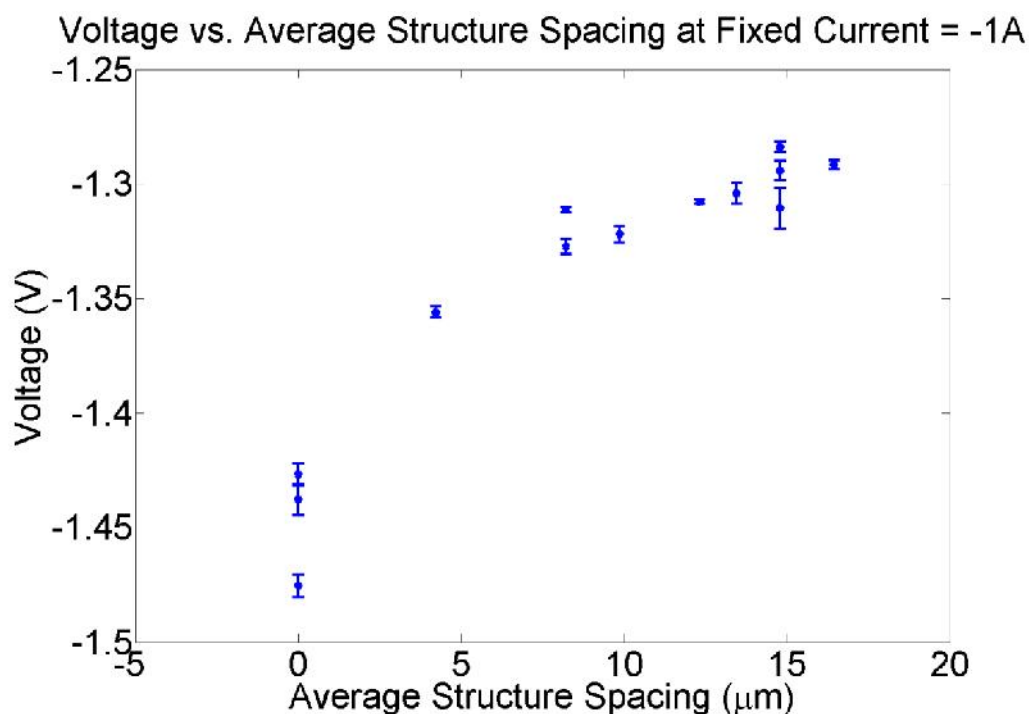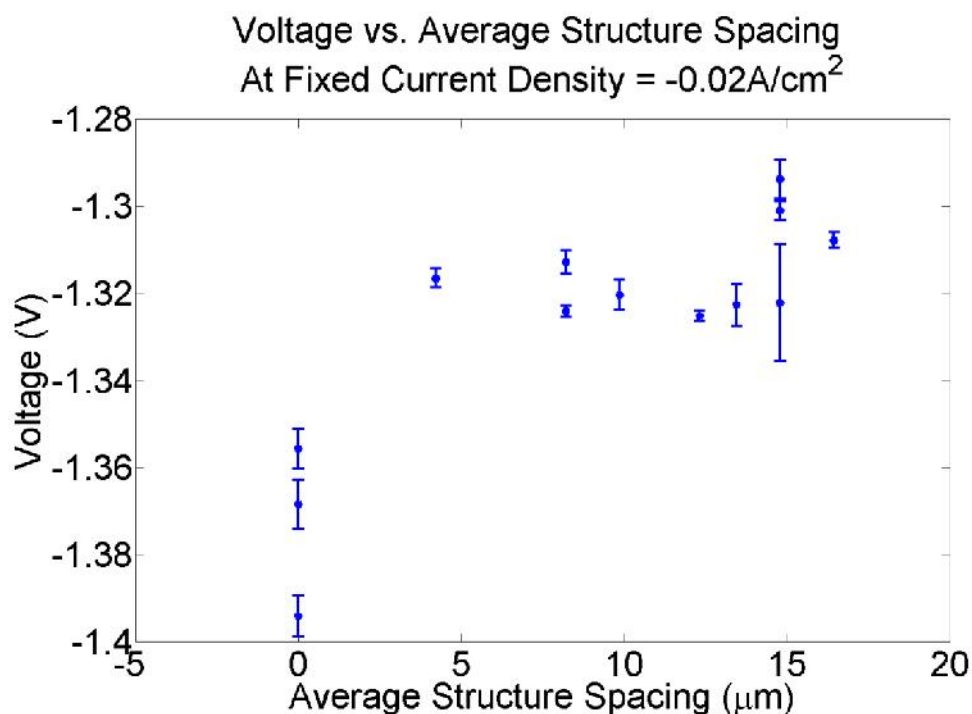
**Figure 28: Relation between the voltage required to reach -1 A/cm$^2$ and the average structure spacing of all electrodes including the polished, plasma cleaned, and FLSP electrodes**

The data presented in Figure 27 and Figure 28 indicate that there is very little difference in the voltage required to produce -0.02 A/cm$^2$ as the average peak to valley height or average structure spacing of the FLSP electrodes increased. These results indicate varying the structure peak to valley height or the structure spacing does decrease the voltage to reach -0.02 A/cm$^2$ as compared to the polished electrode, but the amount of voltage decrease is the same for all structured electrodes, about 79.49 mV. This could yield benefits in preexisting electrolyzers where electrode parameters have been established. Using FLSP on the electrodes would increase the rough surface area of the electrodes and decrease the amount of voltage required to produce a specified current density or yield much larger current values for a given voltage setting, as compared to the polished electrodes.

## 4.3.    Bubble Analysis

Analysis of bubble production on the electrodes was conducted using high speed video capture. A Photron FASTCAM SA1 high speed camera was used to capture video of a polished electrode and FLSP electrode during the onset of bubbles on the surface of the electrodes. The rate of video capture was 500 frames per second. Bubbles were generated on the surface of the electrode using a two electrode cell with optically clear acrylic walls. The surface of the working electrode was normal to the camera lens and the counter electrode was position so that it did not impede the view of the working electrode. A 1M KOH(aq) solution was used as the electrolyte. A power supply generating 200 mA of current supplied to the cell. The electrodes were made of 316 SS and the FLSP electrode was created prior to the grid presented in Sections 4.1 and 4.2. The parameters used to create this electrode were not recorded. Images stills from the resulting videos can be found in Figure 29.
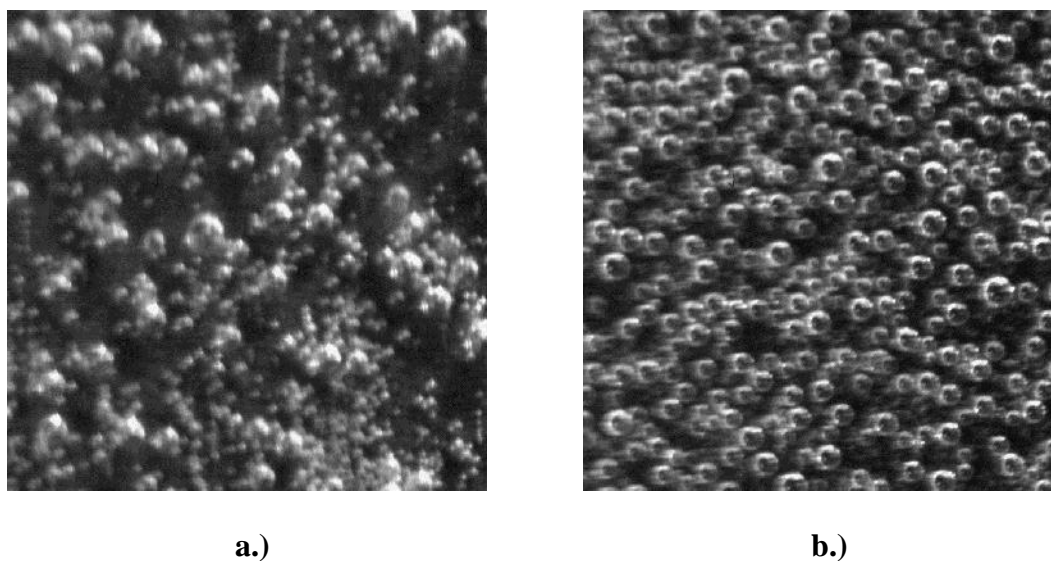


a.)                                                          b.)

**Figure 29: Image stills from highspeed video of a.) a polished 316 SS electrode and b.) a FLSP 316 SS electrode**

The stills in Figure 29 were taken once the initial wave of bubbles had released. It can be seen that the bubbles on the FLSP electrode were smaller and denser than the bubbles created on the polished electrode. The Matlab program used to analyze the FLSP surface structure spacing was used on the bubbles to measure bubble density and size, but issues were presented with overlapping bubbles and bubbles produced at the electrode edges. The overlapping bubbles caused the program to register them as one and skewing the bubble size and density measurements. The bubbles produced at the electrode edges were larger than those produced on the surface of the electrode. These bubbles would sweep past the bubbles on the electrode surface causing them to release prematurely or combine with the bubbles.

The visual analysis of the bubbles produced on the electrode surfaces verify that the bubbles produced on the electrode surface are smaller than those on the polished surface and release faster, but it does not indicate if the total amount of gas produced from the FLSP electrode is greater than the polished electrode. If this analysis was performed on the electrodes created in the previously studied grid, a better understanding of how the bubbles produced on the FLSP electrodes influence the LSV behavior could be developed.

# Chapter 5.    Conclusions

Femtosecond laser surface processing was used to enhance the surface of a 316 stainless steel metal plate for application in water electrolysis with the purpose of creating hydrogen and oxygen gas. The purpose of this series of studies was to determine the effects that the FLSP induced multi-scale structured surface had on the hydrogen

production capabilities of an industry common material without the addition of a secondary material. Initial results indicated that the structured surfaces decreased the amount of voltage required to initiate the electrochemical reaction. The magnitude of voltage reduction seemed dependent on the height, size, and density of the structures present on the electrode surface. Multiple experiments were conducted to determine the cause of the reduction in voltage.

Surface area of the electrodes was first investigated to determine if the multi-scale surfaces simply increased surface area, which leads to an increased cell current according to Faraday's Law. It was found that the performance of the FLSP electrodes after normalizing by surface area was similar in terms of LSV behavior, but still appeared more electro-active as compared to the polished electrode. While error was present in the 3D microscopy data of the FLSP electrodes with deep pits, the difference between the polished electrode and the FLSP electrodes with shallow pits indicated that more factors were influencing the electrochemical process.

Effects of wettability on the electrochemical process were investigated next. The polished electrode used for the previous experiments was plasma cleaned using ambient air and pure oxygen. The removal of surface carbons reduced the contact angle of water on the electrode surface from 35° to 9.8°. The reduction in surface wettability caused a shift in LSV performance of the polished electrode closer to the performance of the FLSP electrodes, but did not match the performance exactly. Plasma cleaning was conducted on a FLSP electrode to ensure that factors other than surface wettability were not affected by the plasma cleaning and performance of the FLSP would not change. It was found that

the FLSP and plasma-cleaned FLSP electrode contact angles were no different and LSV performance were the exact same.

Electron transfer of the FLSP electrodes was investigated last. Existence of linear sections at high potentials in the Tafel plot indicate that the electrochemical reactions between the 316 SS electrodes and the 3 M KOH(aq) solution were predominantly limited by the electron transfer rate. Analysis of the Tafel behavior indicated that the electron transfer mechanism was the same between all FLSP electrodes, polished electrodes, and plasma cleaned electrodes. This suggests that the surface chemistry of the electrodes is not affected by FLSP or any changes were not significant to the electrochemical process.

Investigation of these three topics shows that FLSP on electrodes increases surface area, increases surface wettability, but does not change the electron transfer mechanism of the electrode/electrolyte interface. Factoring out the effects of surface area and wettability show that there is another factor beyond those investigated that causes the FLSP electrodes to perform better than the polished, plasma cleaned electrodes. Vogt [31, 33] suggests that this factor is, in part, the nucleation site and the effect on bubble formation size and size upon release. The work presented shows that FLSP electrodes can be used to reduce the potential required to generate current in an electrochemical cell by up to 191 mV at -1A.

## 5.1. Future Work

The biggest improvement to this study would be to analyze the bubbles that are forming on the surface of the electrodes prior to and at release of both the electrodes. It is

expected that the bubbles formed on the FLSP electrodes spend less time on the electrode surface and release at a smaller diameter. This will allow more of the working electrode to be continuously involved in the reaction. A method must be developed to determine when and how bubble diameter should be measured. One challenge that must be overcome is bubble size detection. Upon current flow, bubbles are created over the entire surface of the electrode and are released at about the same time. Bubbles that have released early will rise up and block the view of bubbles that are still developing on the surface of the electrode.

A proposed solution would be to image the entire surface of the electrode to identify which nucleation sites are releasing bubbles first, but the size of a majority of the bubbles require a macro lens to image and the field of view is limited. Another suggestion is to use smaller electrodes for the purpose of bubble visualization. Another related challenge that must be overcome is to determine when a bubble should be measured. Vogt [31, 33] identifies the importance of bubble diameter upon release, but identification of the point at which a bubble releases may be difficult due to circulation caused by other bubbles rising, bubbles combining, and difficulty identifying when a bubble releases.

Another improvement that could be made to the study is to use platinum electrodes. Platinum is the most electro-active element available for electrochemistry. Conducting a study using FLSP on a high purity platinum alloy would eliminate the complexity of understanding the effects of FLSP on an alloy and simplify the material composition at the surface. Processing the platinum within a controlled environment, i.e.

pure nitrogen or oxygen atmosphere, would help prevent the issue of oxidation of the multi-scale structures during and after processing.

One area of investigation that could branch out from this work is the use of coatings with the FSLP induced surface structures, specifically atomic layer deposition. It has been suggested that platinum be initially used with these multi-scale surface to combine the high electro-activity of the platinum with the enhanced nucleation sites of the surfaces. An additional benefit that this type of coating may have is to improve the conductivity of the electrode surface. This could reduce the resistance of electron transfer between the electrode and electrolyte and change the behavior of the basic stainless steel electrode. Another benefit of this type of electrode would be cost saving in that the amount of platinum used is limited to just the surface of interest while the base material is significantly less costly.

The studies presented in this thesis have shown that femtosecond laser surface processing greatly enhances the performance of electrodes during water electrolysis. This performance enhancement can be generated without the assistance of surface coatings and without introducing oxidation that would not be found on a polished stainless steel electrode. Optimization of the surface processing techniques and laser parameters could generate electrodes of common material that rivals the performance of platinum electrodes. Combining the FLSP technique with surface coatings would push the boundaries of enhancements in electrochemistry.

# References

[1]     E. Zoulias and E. Varkaraki, "A review on water electrolysis," *TCJST*, pp. 41–71, 2004.

[2]     K. Zeng and D. Zhang, "Recent progress in alkaline water electrolysis for hydrogen production and applications," *Prog. Energy Combust. Sci.*, vol. 36, no. 3, pp. 307–326, Jun. 2010.

[3]     S. Trasatti, "Water electrolysis: who first?," *J. Electroanal. Chem.*, vol. 476, no. 1, pp. 90–91, Oct. 1999.

[4]     W. Kreuter and H. Hofmann, "Electrolysis: the important energy transformer in a world of sustainable energy," *Int. J. Hydrogen Energy*, vol. 23, no. 8, 1998.

[5]     K. Onda, T. Kyakuno, K. Hattori, and K. Ito, "Prediction of production power for high-pressure hydrogen by high-pressure water electrolysis," *J. Power Sources*, vol. 132, no. 1–2, pp. 64–70, May 2004.

[6]     F. Ye, J. Li, X. Wang, T. Wang, S. Li, H. Wei, Q. Li, and E. Christensen, "Electrocatalytic properties of Ti/Pt–IrO2 anode for oxygen evolution in PEM water electrolysis," *Int. J. Hydrogen Energy*, vol. 35, no. 15, pp. 8049–8055, Aug. 2010.

[7]     M. Carmo, D. L. Fritz, J. Mergel, and D. Stolten, "A comprehensive review on PEM water electrolysis," *Int. J. Hydrogen Energy*, vol. 38, no. 12, pp. 4901–4934, Apr. 2013.

[8]     D. F. Call, M. D. Merrill, and B. E. Logan, "High surface area stainless steel brushes as cathodes in microbial electrolysis cells.," *Environ. Sci. Technol.*, vol. 43, no. 6, pp. 2179–83, Mar. 2009.

[9]     P. a. Selembo, M. D. Merrill, and B. E. Logan, "Hydrogen production with nickel powder cathode catalysts in microbial electrolysis cells," *Int. J. Hydrogen Energy*, vol. 35, no. 2, pp. 428–437, Jan. 2010.

[10]    G. R. Bamwenda, S. Tsubota, T. Nakamura, and M. Haruta, "Photoassisted hydrogen production from a water-ethanol solution: a comparison of activities of Au    TiO2 and Pt    TiO2,"*J. Photochem. Photobiol. A Chem.*, vol. 89, no. 2, pp. 177–189, Jul. 1995.

[11]    J. Moir, N. Soheilnia, P. O'Brien, A. Jelle, C. M. Grozea, D. Faulkner, M. G. Helander, and G. a Ozin, "Enhanced hematite water electrolysis using a 3D antimony-doped tin oxide electrode.," *ACS Nano*, vol. 7, no. 5, pp. 4261–74, May 2013.

[12]    M. Ni, M. K. H. Leung, D. Y. C. Leung, and K. Sumathy, "A review and recent developments in photocatalytic water-splitting using TiO2 for hydrogen production," *Renew. Sustain. Energy Rev.*, vol. 11, no. 3, pp. 401–425, Apr. 2007.

[13]   M. S. El-Deab and T. Ohsaka, "Manganese oxide nanoparticles electrodeposited on platinum are superior to platinum for oxygen reduction.," *Angew. Chem. Int. Ed. Engl.*, vol. 45, no. 36, pp. 5963–6, Sep. 2006.

[14]   L. Feng, H. Vrubel, M. Bensimon, and X. Hu, "Easily-prepared dinickel phosphide (Ni2P) nanoparticles as an efficient and robust electrocatalyst for hydrogen evolution.," *Phys. Chem. Chem. Phys.*, vol. 16, no. 13, pp. 5917–21, Apr. 2014.

[15]   C. G. Morales-Guio, S. D. Tilley, H. Vrubel, M. Grätzel, and X. Hu, "Hydrogen evolution from a copper(I) oxide photocathode coated with an amorphous molybdenum sulphide catalyst.," *Nat. Commun.*, vol. 5, no. I, p. 3059, Jan. 2014.

[16]   K. Oldham and J. Myland, *Fundamentals of Electrochemical Science*, 1st ed. London: Academic Press, 1994.

[17]   J. Böckris and A. Reddy, *Modern Electrochemistry 1*, 2nd Editio. New York: Kluwer Academic Publishers, 1998.

[18]   D. Santos, C. Sequeira, and J. Figueiredo, "Hydrogen production by alkaline water electrolysis," *Quim. Nova*, vol. 36, no. 8, pp. 1176–1193, 2013.

[19]   T. R. Gilbert, R. V. Kirss, N. Foster, and G. Davies, *Chemistry*, 3rd ed. New York: W.W. Norton & Company, 2012.

[20]   A. Bard and L. Faulkner, *Electrochemical Methods: Fundamentals and Applications*, 2nd ed. New Delhi: Wiley, 2006, p. 27.

[21]   T. Jaramillo, K. Jørgensen, and J. Bonde, "Identification of active edge sites for electrochemical H2 evolution from MoS2 nanocatalysts," *Science (80-. ).*, vol. 317, no. 5834, pp. 100–102, 2007.

[22]   Y.-J. Huang, C.-H. Lai, P.-W. Wu, and L.-Y. Chen, "Ni Inverse Opals for Water Electrolysis in an Alkaline Electrolyte," *J. Electrochem. Soc.*, vol. 157, no. 3, p. P18, 2010.

[23]   S. Ben Aoun, Z. Dursun, T. Sotomura, and I. Taniguchi, "Effect of metal ad-layers on Au(111) electrodes on electrocatalytic reduction of oxygen in an alkaline solution," *Electrochem. commun.*, vol. 6, no. 8, pp. 747–752, Aug. 2004.

[24]   C. Fan, D. Piron, A. Sleb, and P. Paradis, "Study of Electrodeposited Nickel-Molybdenum, Nickel-Tungsten, Cobalt-Molybdenum, and Cobalt-Tungsten as Hydrogen Electrodes in Alkaline Water Electrolysis," *J. Electrochem. Soc.*, vol. 141, no. 2, pp. 382–387, 1994.

[25]   M. S. El-Deab, M. I. Awad, A. M. Mohammad, and T. Ohsaka, "Enhanced water electrolysis: Electrocatalytic generation of oxygen gas at manganese oxide nanorods modified electrodes," *Electrochem. commun.*, vol. 9, no. 8, pp. 2082–2087, Aug. 2007.

[26]     S. Kim, N. Koratkar, T. Karabacak, and T.-M. Lu, "Water electrolysis activated by Ru nanorod array electrodes," *Appl. Phys. Lett.*, vol. 88, no. 26, p. 263106, 2006.

[27]     D. Menshykau and R. G. Compton, "The Influence of Electrode Porosity on Diffusional Cyclic Voltammetry," *Electroanalysis*, vol. 20, no. 22, pp. 2387–2394, Nov. 2008.

[28]     D. Menshykau, I. Streeter, and R. G. Compton, "Influence of Electrode Roughness on Cyclic Voltammetry," *J. Phys. Chem. C*, vol. 112, no. 37, pp. 14428–14438, Sep. 2008.

[29]     F. Scholz, *Electroanalytical Methods: Guide to Experiments and Applications*, 2nd ed. New York: Springer, 2010.

[30]     S. Jones, G. Evans, and K. Galvin, "Bubble nucleation from gas cavities—a review," *Adv. Colloid Interface Sci.*, pp. 27–50, 1999.

[31]     H. Vogt and R. J. Balzer, "The bubble coverage of gas-evolving electrodes in stagnant electrolytes," *Electrochim. Acta*, vol. 50, no. 10, pp. 2073–2079, Mar. 2005.

[32]     J. Eigeldinger and H. Vogt, "The bubble coverage of gas-evolving electrodes in a flowing electrolyte," *Electrochim. Acta*, vol. 45, no. 27, pp. 4449–4456, Sep. 2000.

[33]     H. Vogt, "The actual current density of gas-evolving electrodes—Notes on the bubble coverage," *Electrochim. Acta*, vol. 78, pp. 183–187, Sep. 2012.

[34]     *Tsunami Mode-locked Ti:sapphire Laser User's Manual*, no. 0000. Spectra-Physics, 2002.

[35]     *Spitfire, 50 fs, 1 kHz User Manual*. Spectra-Physics, 2002.

[36]     K. Wall and A. Sanchez, "Titanium sapphire lasers," *Lincoln Lab. J.*, vol. 3, no. 3, pp. 447–462, 1990.

[37]     W. Koechner and M. Bass, *Solid-State Lasers: A Graduate Text*. 2003.

[38]     J. Schiffern, "Enhancement of Femtosecond Laser-induced Breakdown Spectroscopy for the Nanomorphing/stratigraphy of Biological Samples," 2007.

[39]     C. Zuhlke, T. Anderson, and D. Alexander, "Formation of multiscale surface structures on nickel via above surface growth and below surface growth mechanisms using femtosecond laser pulses," *Opt. Express*, vol. 21, no. 7, pp. 97–98, 2013.

[40]     C. a. Zuhlke, T. P. Anderson, and D. R. Alexander, "Fundamentals of layered nanoparticle covered pyramidal structures formed on nickel during femtosecond laser surface interactions," *Appl. Surf. Sci.*, vol. 283, pp. 648–653, Oct. 2013.

[41]     C. Zuhlke, *Control and understanding of the formation of micro/nanostructured metal surfaces using femtosecond laser pulses*. 2012.

[42]     *VersaSTAT 3 Hardware Manual*. Princeton Applied Research.

[43]   B. Kinkead, J. Drunen, M. T. Y. Paul, K. Dowling, G. Jerkiewicz, and B. D. Gates, "Platinum Ordered Porous Electrodes: Developing a Platform for Fundamental Electrochemical Characterization," *Electrocatalysis*, vol. 4, no. 3, pp. 179–186, Jul. 2013.

[44]   V. Fragkou and Y. Ge, "Determination of the Real Surface Area of a Screen-Printed Electrode by Chronocoulometry.," *Int. J. Electrochem. Sci.*, vol. 7, pp. 6214–6220, 2012.

[45]   S. Trasatti and O. Petrii, "Real surface area measurements in electrochemistry," *J. Electroanal. Chem.*, vol. 63, no. 5, 1992.

[46]   R. Wüthrich, C. Comninellis, and H. Bleuler, "Bubble evolution on vertical electrodes under extreme current densities," *Electrochim. Acta*, vol. 50, no. 25–26, pp. 5242–5246, Sep. 2005.

[47]   W. Sheng, M. Myint, J. G. Chen, and Y. Yan, "Correlating the hydrogen evolution reaction activity in alkaline electrolytes with the hydrogen binding energy on monometallic surfaces," *Energy Environ. Sci.*, vol. 6, no. 5, p. 1509, 2013.